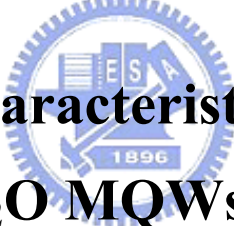# 國 立 交 通 大 學
光 電 工 程 研 究 所

碩士論文

非極性"a"平面氧化鋅多重量子井結構之光學特性

Optical Characteristics of a-plane ZnO/Zn$_{0.8}$Mg$_{0.2}$O MQWs grown by Pulsed Laser Deposition

研究生：卓立夫

指導教授：郭浩中教授

盧廷昌教授

中華民國九十八年七月

非極性"a"平面氧化鋅多重量子井結構之光學特性

Optical Characteristics of a-plane ZnO/Zn$_{0.8}$Mg$_{0.2}$O MQWs

grown by Pulsed Laser Deposition

研究生：卓立夫　　　　　　　　　Student: Li. Fu. Zhuo

指導教授：郭浩中 教授　　　　　　Advisor: Prof. Hao-chung Kuo

盧廷昌 教授　　　　　　　　　　　Prof. Tien-chang Lu

國 立 交 通 大 學 電機資訊學院

光電工程研究所

碩 士 論 文

A Thesis

Submitted to Institute of Electro-Optical Engineering

College of Electrical Engineering and Computer Science

National Chiao Tung University

in Partial Fulfillment of the Requirements

for the Degree of

Master

In

Electro-Optical Engineering

July 2009

Hsinchu, Taiwan, Republic of China

中 華 民 國 九十八 年 七 月

非極性"a"平面氧化鋅多重量子井結構之光學特性

研究生:卓立夫　　　　　　　　　　指導教授:郭浩中 教授

盧廷昌 教授

國立交通大學光電工程研究所

摘要

在本篇論文中，我們利用脈衝雷射蒸鍍製程技術成長不同的非極性"a"平面氧化鋅/氧化鋅鎂多重量子井作為研究對象。在特性分析中，包含了結構與光學特性上的相關研究。在發光特性方面，所利用的是光激發螢光光譜(PL)，以及吸收光譜(absorption spectra)技術進行樣品的光學特性分析,結構及相關成分的研究包含了穿透式電子顯微鏡圖像、能量散佈光譜、選區繞射…。

在低溫 PL 可以觀察到比較薄的量子井有較高的量子侷限效應,同時在變功率的 PL 實驗中,發現樣品的發光波長並不隨者雷射功率增加而改變,意味者非極性面成長的氧化鋅多重量子井確實有效的抑制了 QCSE 的效應。從變溫PL 的光譜變化顯示激子有效的侷限在量子井中以及藉由變溫PL 的曲線擬合的結果可以得到激子的束縛能有效的提高。成長非極性結構的另一優勢在於極化發光(polarized light emission)的價值,我們所測得的發光極化率大約在93%左右(@20K)。偏振的吸收光譜解析出了價電帶的能帶位置,而第一個價電帶和第二個價電帶的能量差正是使得氧化鋅的多重量子井有高極化率的主因。

將雷射聚焦到微米等級,並且使用 YVO4 脈衝雷射去光激發我們的樣品可以觀察到氧化鋅非線性光學的發光現象。在極高的雷射能量密度下光激發,觀察到了電子電洞所形成離子團的發光特性,並且出現了 random lasing 的特殊現象,此種不需要反射鏡即可產生半高寬小於 0.37nm 的光源,值得未來更進一步的開發成電激發的光電雷射元件。

Optical Characteristics of a-plane ZnO/Zn$_{0.8}$Mg$_{0.2}$O MQWs grown by Pulsed Laser Deposition

Student: Li Fu Zhuo   Advisors: Prof. Hao-chung Kuo

Prof. Tien-chang Lu

Institute of Electro-Optical Engineering, National Chiao Tung University

Abstract

In this thesis, a-plane ZnO/ZnMgO multiple quantum wells were grown on r-plane sapphire by pulsed laser deposition for investigation. We utilized several methods including photoluminescence (PL), polarized absorption spectra, and micro photoluminescence (μ-PL) to investigate the optical characteristics of our samples.

Energy dispersive spectrometer revealed the magnesium concentration of barrier layer is 20%. Transmission electronic microscopy was further carried out to determine the growth direction of MQWs along [11-20] and the barrier and well thicknesses.

The low temperature PL experiments revealed that the larger quantum confinement in thinner quantum well. Meanwhile, the power dependent PL measurement indicated no apparent emission peak shift for all samples due to no built-in electric field in a-plane MQWs. Moreover, the temperature dependent PL reveals that excitons were confined well in MQWs. From the fitting result of activation energy, the exciton binding energy was further enhanced by quantum well. High degree polarization ratio (92%) was observed in ZnO/Zn$_{0.8}$Mg$_{0.2}$O MQWs (@20K). From the polarized absorption spectra experiment results, electronic band

structure was observed. Larger $\triangle$E (E2-E1) was the main reason which induced high

polarization ratio. Further, we demonstrated the random lasing behavior of a-plane

ZnO/ZnMgO MQWs. At high excitation intensity (~55.7MWcm^{-2}), many sharp peaks

emerge on the spectra. The FWHM of each individual peaks was about 0.37nm and

the mode spacing was about 0.65nm. From the equation we had calculated the exciton

binding energy is around 66meV which is closed to the activation energy. We

attributed this lasing behavior from the forming of electron-hole plasma and the

threshold was about 47.33MWcm^{-2}. For constant pump intensity of 113 MWcm^{-2},

larger excitaition area produces EHP lasing behavior easier. This is also a

characteristic behavior in random lasing system.

Acknowledgement

碩士班的兩年實在過的非常的快，沒想到竟然輪到我畢業了，回頭看看這兩年，真得是充滿者歡笑與淚水阿!!!首先，一定要先感謝我們實驗室的三位老師:王老師，郭老師，盧老師。王老師每次爽朗的笑容總是讓大家歡樂許多，郭老師對我們的要求，讓我們知道碩士班的學生應該要做到什麼樣的水準，盧老師對實驗的挑剔，讓我知道做實驗以及分析數據應該要保持什麼樣的態度，相信未來三位老師們一定能帶領實驗室為台灣做出更多更好的研究成果。

謝謝宗憲學長對我的指導，學長的遠見以及對實驗方向的獨特嗅覺，使得我不用浪費很多時間，而能很有效的解決問題。除了實驗方面學長對於我做人處事方面也指導許多，讓我做人更圓融，更懂得怎麼看人。

第二個幫助我最多的人就是俊榮學長，你雖然給我的意見不多，但都是很關鍵的幾個癥結。平常俊榮對學弟妹的照顧實在是揪甘心ㄟ!!!。小閔學長做事非常細心，我們總是一起煩惱小咪要報告什麼，一起討論一些問題，不過我要先你一步走了，保重阿。

玫君，你常常削水果請我們吃，碩一的時候我們一起完成了很多困難的作業，希望我們兩個都能減肥成功，小楊，雖然我不愛喝酒不愛吃宵夜，不過我還是很樂意陪你聊天的，你的用語實在讓我們津津樂道阿!阿綱、小馬、智凱、小柯、政暐、QQ，很開心跟你們做同學，祝你們都順順利利的以後常聯絡阿。

實驗室的學弟妹們也幫助我很多，福吉雖然我很喜歡開你玩笑，不過你知道我是打打嘴砲的，歐黃你太沒有個性了，不要再當爛好人了，硬起來吧!阿淇仔你做事看起來很大膽其實你的內心是很纖細的，以後多多照顧歐黃吧，大衛平常找你打球，你都非常阿莎力，真得是我很好的打球咖。

最後感謝謝老師實驗室的學長們，尤其是小郭學長，真得給了我很多的幫助，要感謝的人實在太多了，不如就謝天吧，祝我的朋友們都順順利利的，大家加油。

Content

List of Figures

Chapter 1 Introduction and Motivation

1.1 Introduction to opto-electronic material

Nowadays, blue and UV light emitted diodes with efficiency, brightness, and longevity that are well in excess of those required for outdoor applications are highly expectable. With full of vital development of LEDs, LEDs have a variety of applications in the different field. Among the applications of them are indicator lights, signs, traffic lights, background lighting source of liquid crystal display, and lighting which requires emission in the visible part of the spectrum…..etc.. Nevertheless, the current LEDs might have difficulties in the hard growth, low light efficiency, and large energy loss, which results in LEDs in the application of lighting are not good enough to replace the traditional fluorescent light. Potentially, further improvement in LEDs would be definitely required for the future life.

In recent years, the desire for blue and UV diode lasers and light emitting diodes has prompted enormous research efforts into II–VI and III–V wideband gap semiconductors. Among the well-known semiconductor materials employed in various technical applications, two unique positions are held by gallium nitride (GaN) and zinc oxide (ZnO) in the wide direct band gap semiconductor. In the material property, both GaN and ZnO have many similar aspects, such as material structure, lattice constant, energy band gap,… etc.. In the difference of which, the remarkable

property of ZnO better than GaN is exciton binding energy of 60 meV, which is only 30 meV for GaN. Owing to the larger exciton binding energy, more excitons exist in the room temperature, resulting in higher luminescence than GaN. Furthermore, ZnO can be grown at lower temperature on the cheaper substrate and lead to low cost of growth. However, because of more intrinsic defects, the hard growth of p-type ZnO to achieve the p-i-n junctions, and the degradation of material quality, the current commercial blue and UV LEDs are primitively composed of GaN. However, GaN-based LEDs still face some problems of the luminescence, such as more defects in the material and low electron-hole recombination of c-direction growth. Therefore, it is worth making the further researches on the material of ZnO and GaN on purpose of possessing well-performed LEDs and LDs.
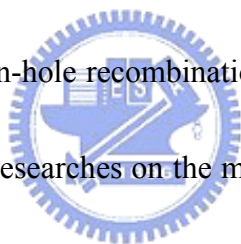
With the concern of growth technique, the material such ZnO is grown on c-plane sapphire, $ScAlMgO_4$ or Si substrate. The growth direction along c-axis could confront a problem that along the carrier flowing direction, because of asymmetric electric charge in the atom, built-in electric field exists in the ZnO material. The causes of the built-in electric field exist two：one is different electric charges carried by group-II and group-VI atoms and another is piezo-electric field resulted from the lattice mismatch between the material and the substrate, which is so-called quantum confined stark effect (QCSE) [1][2]. The field leads to band bending and forces the

carriers to the opposite side of the quantum well. The overlapping probability of the wave function taking place between electrons and holes would decrease, as weaken the lighting efficiency (Fig. 1.1.1).

In the limit of the direction of material growth and polarization resulted from the HCP structure, the efficiency of the opto-electronic transformation is still not enough. New outstanding materials or other directions of growth are definitely required to be investigated in detail. In the aspect of the non-polar plane, besides enhancement of opto-electronic transformation, the emission light from non-polar material is also in possession of the polarization properties, which has a great benefit in the application of opto-electronic device.

1.2   Material characteristics of zinc oxide

In materials science, ZnO is often called a II-VI semiconductor because zinc and oxygen belong to the 2nd and 6th groups of the periodic table, respectively. This semiconductor has several favorable properties: good transparency, high electron mobility, wide band-gap, strong room-temperature luminescence, etc. Those properties are already used in emerging applications for transparent electrodes in liquid crystal displays and in energy-saving or heat-protecting windows, electronic applications of ZnO as thin-film transistor and light-emitting diode are forthcoming as of 2010.

Zinc oxide crystallizes is hexagonal wurtzite (Fig1.2.1). The hexagonal structure has a point group $6°mm$ or C_{6v}, and the space group is $P6_3mc$ or C_{6v}^4. The lattice constants are a = 3.25 Å and c = 5.2 Å; their ratio c/a ~ 1.60 is close to the ideal value for hexagonal cell c/a = 1.633. As in most II-VI materials, the bonding in ZnO is largely ionic, which explains its strong piezoelectricity. Due to this ionicity, zinc and oxygen planes bear electric charge (positive and negative, respectively).

ZnO has a relatively large direct band gap of ~3.3 eV at room temperature; therefore, pure ZnO is colorless and transparent. Advantages associated with a large band gap include higher breakdown voltages, ability to sustain large electric fields, lower electronic noise, and high-temperature and high-power operation. The bandgap of ZnO can further be tuned from ~3–4 eV by its alloying with magnesium oxide or cadmium oxide.

Most ZnO has n-type character, even in the absence of intentional doping. Native defects such as oxygen vacancies or zinc interstitials are often assumed to be the origin of this, but the subject remains controversial. An alternative explanation has been proposed, based on theoretical calculations, that unintentional substitutional hydrogen impurities are responsible. Controllable n-type doping is easily achieved by substituting Zn with group-III elements Al, Ga, In or by substituting oxygen with group-VII elements chlorine or iodine. Reliable p-type doping of ZnO remains

difficult. This problem originates from low solubility of p-type dopants and their compensation by abundant n-type impurities, and it is pertinent not only to ZnO, but also to similar compounds GaN and ZnSe. Measurement of p-type in "intrinsically" n-type material is also not easy because in-homogeneity results in spurious signals.

Current absence of p-type ZnO does limit its electronic and optoelectronic applications which usually require junctions of n-type and p-type material. Known p-type dopants include group-I elements Li, Na, K; group-V elements N, P and As well as copper and silver. However, many of these form deep acceptors and do not produce significant p-type conduction at room temperature.
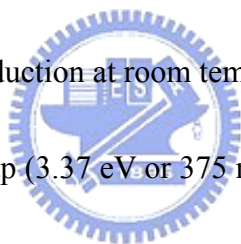
ZnO has wide direct band gap (3.37 eV or 375 nm at room temperature). Therefore, it's most common potential applications are in laser diodes and light emitting diodes (LEDs). Some optoelectronic applications of ZnO overlap with that of GaN, which has a similar bandgap (~3.4 eV at room temperature). Compared to GaN, ZnO has a larger exciton binding energy (~60 meV, 2.4 times of the room-temperature thermal energy), which results in bright room-temperature emission from ZnO. Recent studies of ZnO epilayers have observed spontaneous emission from free-exciton (FE) radiative recombination as well as stimulated emission from exciton-exciton scattering (EES) and electron-hole-plasma (EHP) radiative recombination at temperature up to ~550K.[3] Other properties of ZnO favorable for electronic

applications include its stability to high-energy radiation and to wet chemical etching.

The pointed tips of ZnO nanorods result in a strong enhancement of an electric field.

Therefore, they can be used as field emitters. Transparent thin-film transistors (TTFT)

can be produced with ZnO. As field-effect transistors, they even may not need a p–n

junction, thus avoiding the p-type doping problem of ZnO. Some of the field-effect

transistors even use ZnO nanorods as conducting channels.

1.3   Fabrication of nanostructure materials

Low dimension structure as the active layer was widely applied in these optical

devices to operate in low threshold current, reduce temperature sensitivity and

enhance the emitting efficiency due to quantum confine effect [4-5]. Because of the

different dimensional confinement of carrier and density of state, the nanostructure

can be classify into quantum well (QW), nanowire and quantum dot (QD) by their

density of state as shown in Fig. 1.3.1. The bulk material has three dimensional

density of state and the shape is parabolic function, the energy state of carrier is

continues above energy band-gap. Then two dimensional structures, such as quantum

well, is a step function due to one dimensional confinement of carrier. With

decreasing the degree of freedom of carriers, the density of state of zero-dimensional

structure, as quantum dot, manifest delta function density of state. As a result, the

electronic states are quantized and the energy levels become discrete. In Figure 1.3.2,
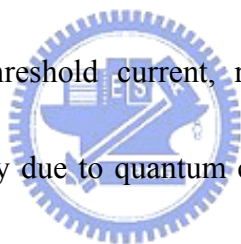
we could see the carriers are localized in the quantum dot structure of three dimensional confinements. There are some unique characteristics in the quantum dot structures. Discrete energy state is an attractive benefit applied to decrease the half of full width in emitting spectrum and separate the different quantum state level. The lasing behavior and quantum information analysis can be improved by their development.

1.4 Motivation of a-plane ZnO / ZnMgO MQWs structure

Huang et al [10] had demonstrated ZnO Nanowires Laser at room temperature in 2001. The lasing threshold is about $40kWcm^{-2}$. They had displayed the feasibility of making ZnO nanolaser. *Kawasaki et al* [11] made the first blue light-emitting diode based on ZnO. Zno is potential materials for making short-wavelength LEDs and diode lasers have been attracting increasing interest as the demands for display, illumination and information storage grow. *Chu et al* [12] reported Sb-doped p-type ZnO/Ga-doped n-type ZnO with an MgZnO/ZnO/MgZnO quantum well embedded in the junction was grown on Si by molecular beam epitaxy. The diodes emit lasing at room temperature with a very low threshold injection current density of 10 A/cm^2. The lasing mechanism is exciton-related recombination and the feedback is provided by close-loop scattering from closely packed nanocolumnar ZnO grains formed on Si.

However, until now (Zn, Mg) O-based heterostructures have been grown in the

[0001] direction only. Unfortunately, the wurtzite ZnO layers exhibit built-in electric fields in this crystallographic orientation, which can be of the order of 1 MV cm^{-1} along the c-axis [13]. The large built-in electric field results in a significant separation of electrons and holes in active layers [14], very long carrier lifetimes and hence very poor light emission efficiencies [15]. The growth on non-polar surfaces such as the A plane (11-20) has, therefore, been proposed to avoid any built-in electric fields, and non-polar QWs have already been demonstrated in GaN-based non-polar heterostructures [16]. Although ZnO is presently intensively studied, very few studies have dealt with ZnO-based nonpolar QW heterostructures until now.

This article is divided into two main sections. Section1 are some basic optical characteristics like power-dependent PL, temperature-dependent PL, polarized absorption spectra…. Section 2 is about the nonlinear optics in Zno/ZnMgO MQWs, and the random lasing behavior in ZnO/ZnMgo MQWs is observed.
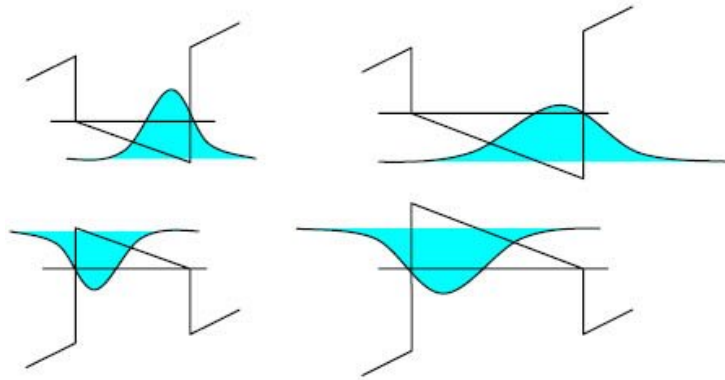
Fig. 1.1.1 Band bending resulted from QCSE in polar quantum well with different

thicknesses
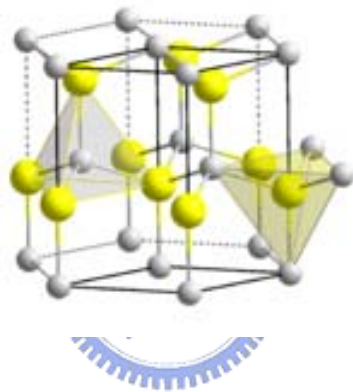
Fig 1.2.1 Crystal structure of Zinc oxide
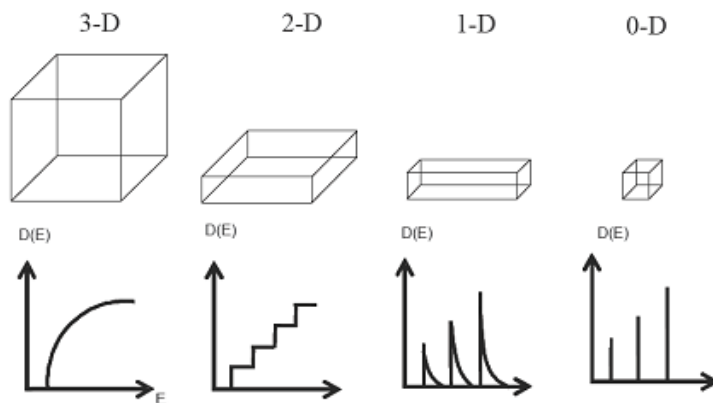
Fig1.3.1 Dimension of nanostructure and corresponding density of state
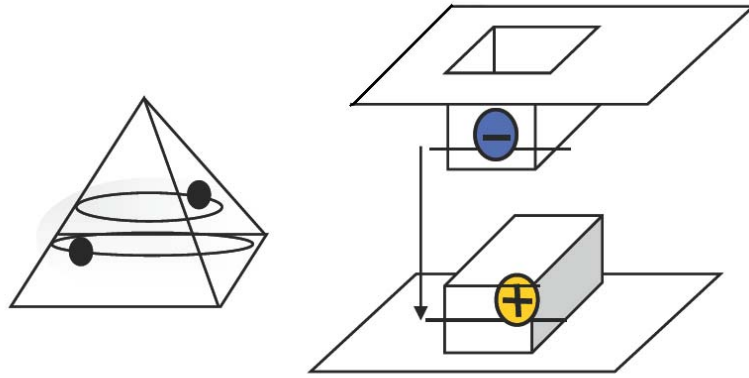
Fig. 1.3.2 The carrier behavior in three dimensional confinement structure

Chapter 2 Properties of nonpolar multiple quantum wells (MQWs) structure

2.1 Quantum confinement effect in semiconductor nanostructure

If we make very small crystals, the optical properties of solids will depend on their size. The size dependence of the optical properties in very small crystals is a consequence of the quantum confinement effect. What "Quantum confinement" means is that when electrons and holes in a semiconductor are restricted in one or two or even three dimensions. For exemple, a quantum dot is confined in all three dimensions, a quantum wire is confined in two dimensions, and a quantum well is confined in one dimension. Therefore, quantum confinement occurs when one or more of the dimensions of a nanostructure are very small so that it approaches the size of an exciton in bulk crystal, called the Bohr exciton radius. [14] In this thesis, we talk about quantum well structure which is a structure where the height is approximately the Bohr exciton radius while the length and breadth in the other two dimensions are relatively free from constraint.

The distance between the electron and the hole is called the effective Bohr radius, a_B of the exciton. When the well width is much larger than a_B in bulk, the exciton binding energy will not show evident difference between the well and the bulk, for the excitons feel nearly the same environment as in bulk. As the well width is decreased

to the order or less than the order of a_B, the wave functions of electrons and holes

overlap get improved and are confined in the well. This also improves the exciton

binding energy.

The Hamiltonian describing the relative motion of the exciton could be written as

$H = H_e(x_e) + H_h(x_h) + H_{e-h}(r)$

where H_e and H_h are the Hamiltonian describing the electron and hole motion

confined in the well. H_{e-h} is the Hamiltonian includes the kinetic energy part of the

relative motion of the exciton in the Y-Z plane and the Coulomb potential attracting

the electron and the hole in the three dimensional form. The x-coordinate of the

electron and hole is denoted as x_e and x_h while r represent the relative position vector

between the electron and the hole. Therefore the eigenvalue solved is given by

$E_n = E^e_{xn} + E^h_{xn} - E_{e-h}$

where E^e_{xn} and E^h_{xn} is the energy of nth quantum confined state, and E_{e-h} is the

binding energy of exciton defined as positive value. Therefore, the lowest exciton

resonance energy associated with the ground state in the quantum well could be

written as $E_{emission} = E_g + E^e_{xn} + E^h_{xn} - E_{e-h}$

The resonance energy was sensitive to well width and the monatomic well size

fluctuation in the narrower well. The well width dependence of the absorption spectra

is determined by competition between the quantum confinement energy level and the

exciton binding energy.

2.2 The basic concept of nonpolar nanostructure

It was from 1994, the use of InGaN/GaN double heterostructure (DH) in LEDs by Nakamura is thought to reignite the III-V nitride system. People did a lot of work in all aspects to improve the light emission efficiency including the material selection、crystal growth、device manufacture process etc. One of the difficulties hampering further advances in nitride emitters is the presence of large piezoelectric fields in these materials.

InGaN/GaN multiple quantum wells are a widely used material and structure to serve as the active layer in nitride heterostructures for its advantage in easy tuning wavelength through controlling the composition of indium. However conventional InGaN/GaN quantum wells grown along the crystallographic c-axis exhibit an internal spontaneous and piezoelectric field in the MV/cm range. The spontaneous field is induced from different atoms arrange in one direction parallel with the growth axis while the piezoelectric field is caused by biaxial compressive strain due to the lattice mismatch between InGaN and GaN.

Under such field, electrons and holes are drawn to opposite interfaces of the QW and the spatial separation of wave functions suppresses radiative recombination with respect to nonradiative recombination, diminishing the emission efficiency drastically.

The built in piezoelectric field also causes a red-shift emission. All the effects caused by the build in electiric field are called as Quantum Confined Stark Effect (QCSE) [17~18]. QCSE becomes severe when the quantum well width gets thicker and indium content is increased. In order to overcome the problem, nonpolar structure was thought as a method to eliminate the built in polarization field. Waltereit and colleagues at the Paul Drude Institute in Berlin first demonstrated the absence of the piezoelectric field in m-plane GaN/AlGaN QWs grown on $LiAlO_2$ substrates [19]. Recently, there have been several approaches to realize nonpolar GaN, m-plane films [24] and m-plane heterostructures [19~20] on γ-$LiAlO_2$(100) as well as a-plane films [25] and a-plane heterostructures [21~23] on r-plane sapphire.The planar relations in hexagonal crystal structure was shown in figure 2.2.1. ZnO and GaN have similar structure, lattice constant, and large band gap. The wurtzite ZnO also have large build in potential if we grown along the [0001] direction.

A schematic energy band diagram between nonpolar quantum well and polar c-plane quantum well under QCSE is shown in figure 2.2.2 (a) (b). As can been seen, the well potential in the nonpolar nanostructure is not influenced by the built in polarization field and possess a higher wavefunction overlap and emission energy than polar nanostructure. Thus nonpolar is now a chance to improve the light emitting efficiency greatly and make a grand breakthrough..

2.3 In-plane light polarization effect in nonpolar nanostructure

In addition to the advantage of no internal electric fields in growth direction, nonpolar orientation of the wurtzite crystal structures are also good for polarization-sensitive devices. In contrast to ZnO films grown along the polar c-plane direction, do not exhibit any in-plane polarization anisotropy, m- and a-plane ZnO films, where the c-axis lies in the film plane, exhibit significant polarization anisotropy in its light emission.

When ZnO films are grown on c-plane substrates with similar hexagonal symmetry, there is no linear polarization emission happened under isotropic in-plane strain. However, a ZnO film with an m-plane or a-plane orientation experience anisotropic in-plane strain resulted from the inherent lower symmetry of m and a plane. An in-plane polarization anisotropy has been observed in the PL spectra of GaN/(Al,Ga)N MQWs. [26, 27]

The coordinate system used for the investigation of the polarization properties is x//a [11-20]、y//m [1−100]、and z//c [0001], the three planes are perpendicular to each other. Take the m-plane GaN films for example, m-plane strain lifts the symmetry in the x-y plane of the wurtzite crystal and separates the original |X±iY>-like HH and LH states of unstrained WZ-GaN to |X>-like and |Y>-like states. A compressive strain along x induces a dilatation along y so that the energy of the |X>-like state is raised

while the |Y>-like state is lowered. Valence bands are reconstituted to |X>-like, |Z>-like, and |Y>-like states in order of decreasing electron energy. Therefore, the valence band structure is altered that the lowest transition energy is totally linearly polarized in the x-direction (E⊥C), while the second lowest transition energy is totally linearly polarized in the z-direction (E∥C). The third lowest transition energy which is linearly polarized in the y-direction will not show any PL intensity difference when we put the polarizer in x-z plane to get the polarization information.

The optical polarization anisotropy in ZnO films with a nonpolar orientation can be used for polarization-sensitive photodetectors [28] and static as well as dynamic polarization filtering [29].
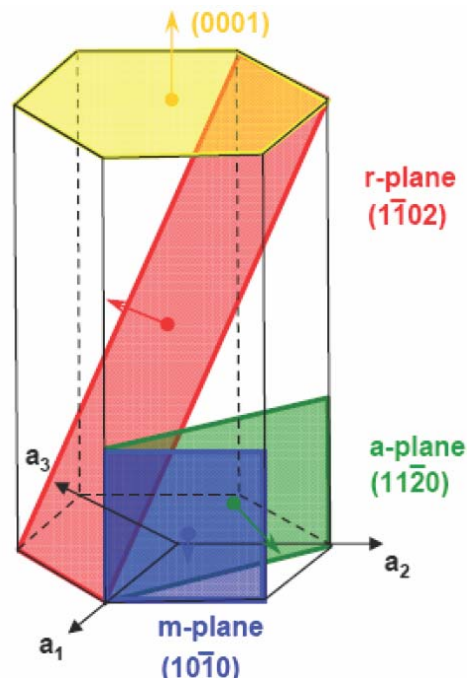
Fig. 2.2.1 The planar relation and orientation in hexagonal crystal structure
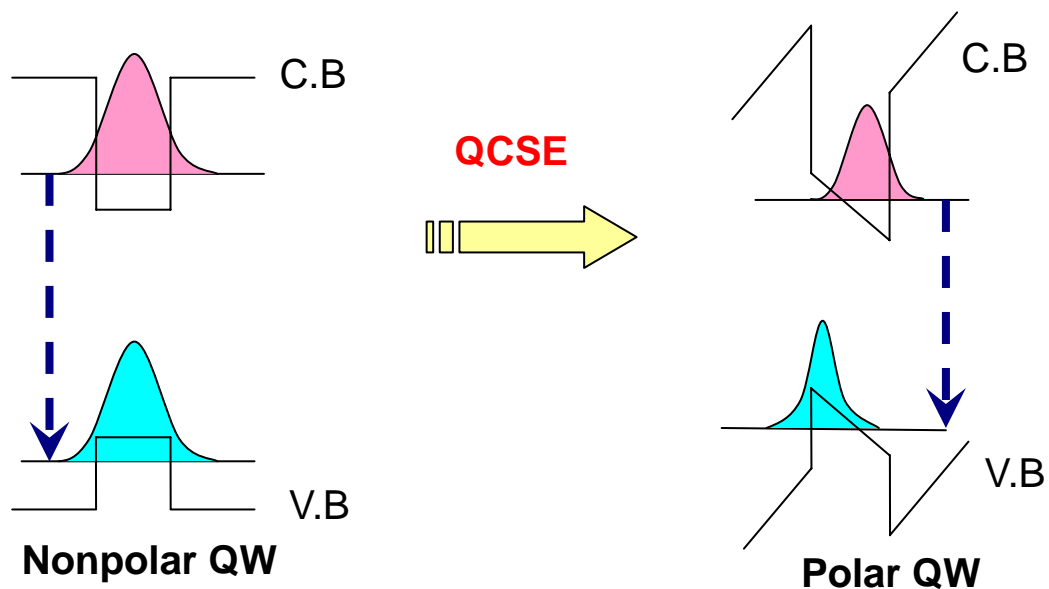
Fig 2.2.2 A schematic energy band diagram of (a) nonpolar quantum well and (b)

polar quantum well under QCSE.

Chapter 3   Theoretical background and experiment apparatus

3.1 Growth mechanism of ZnO/ZnMgO MQWs using pulsed laser deposition (PLD)

The principle of pulsed laser deposition, in contrast to the simplicity of the system

set-up, is a very complex physical phenomenon. It does not only involve the physical

process of the laser-material interaction of the impact of high-power pulsed radiation

on solid target, but also the formation plasma plume with high energetic species and

even the transfer of the ablated material through the plasma plume onto the heated

substrate surface. Thus the thin film formation process in PLD generally can be

divided into the following four stages.

1. Laser radiation interaction with the target

2. Dynamic of the ablation materials

3. Deposition of the ablation materials with the substrate

4. Nucleation and growth of a thin film on the substrate surface

In the first stage, the laser beam is focused onto the surface of the target. At

sufficiently high flux densities and short pulse duration, all elements in the target are

rapidly heated up to their evaporation temperature. Materials are dissociated from the

target surface and ablated out with stoichiometry as in the target. The instantaneous

ablation rate is highly dependent on the fluences of the laser shining on the target. The

ablation mechanisms involve many complex physical phenomena such as collisional,

thermal, and electronic excitation, exfoliation and hydrodynamics.

During the second stage the emitted materials tend to move towards the substrate according to the laws of gas-dynamic and show the forward peaking phenomenon. R. K. Singh reported that the spatial thickness varied as a function of cos q. The spot size of the laser and the plasma temperature has significant effects on the deposited film uniformity. The target-to-substrate distance is another parameter that governs the angular spread of the ablated materials. Hanabusa also found that a mask placed close to the substrate could reduce the spreading.

The third stage is important to determine the quality of thin film. The ejected high-energy species impinge onto the substrate surface and may induce various type of damage to the substrate. The mechanism of the interaction is illustrated in the following figure. These energetic species sputter some of the surface atoms and a collision region is formed between the incident flow and the sputtered atoms. Film grows after a thermalized region is formed. The region serves as a source for condensation of particles. When the condensation rate is higher than the rate of particles supplied by the sputtering, thermal equilibrium condition can be reached quickly and film grows on the substrate surface at the expenses of the direct flow of the ablation particles and the thermal equilibrium obtained.

Nucleation-and-growth of crystalline films depends on many factors such as the

density, energy, ionization degree, and the type of the condensing material, as well as the temperature and the physical-chemical properties of the substrate. The two main thermodynamic parameters for the growth mechanism are the substrate temperature T and the supersaturation D_m. They can be related by the following equation

$$D_m = kT \ln(R/R_e)$$

where k is the Boltzmann constant, R is the actual deposition rate, and R_e is the equilibrium value at the temperature T.

The nucleation process depends on the interfacial energies between the three phases present - substrate, the condensing material and the vapor. The minimum-energy shape of a nucleus is like a cap. For the large nuclei, a characteristic of small supersaturation, they create isolate patches (islands) of the film on the substrate which subsequently grow and coalesce together. As the supersaturation increases, the critical nucleus shrinks until its height reaches on atomic diameter and its shape is that of a two-dimensional layer. For large supersaturation, the layer-by-layer nucleation will happen for incompletely wetted foreign substrates.

The crystalline film growth depends on the surface mobility of the adatom (vapour atoms). Normally, the adatom will diffuse through several atomic distances before sticking to a stable position within the newly formed film. The surface temperature of the substrate determines the adatom's surface diffusion ability. High

temperature favours rapid and defect free crystal growth, whereas low temperature or large supersaturation crystal growth may be overwhelmed by energetic particle impingement, resulting in disordered or even amorphous structures.

In the PLD process, due to the short laser pulsed duration (~10 ns) and hence the small temporal spread (<=10 ms) of the ablated materials, the deposition rate can be enormous (~10 mm/s). Consequently a layer-by-layer nucleation is favoured and ultra-thin and smooth film can be produced. In addition the rapid deposition of the energetic ablation species helps to raise the substrate surface temperature. In this respect PLD tends to demand a lower substrate temperature for crystalline film growth. (Fig3.1.1)
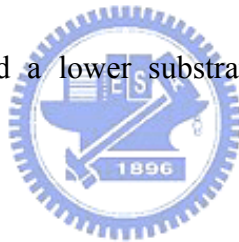
3.2 Transmission Electron Microscope, Energy Dispersive X-ray Spectroscopy (EDS) and Selected Area Electron Diffraction (SAED)

1. Transmission Electron Microscope

Transmission electron microscope is the pre-eminent method for determining dislocation' and other crystallographic defects character and for performing chemical and crystallographic analysis of micrometer and smaller precipitates and other microstructures. With the similar structure and more powerful function compared with SEM, TEM offers the in-depth perspective of specimen characterizations.

Any TEM is a complex assembly of magnetic lenses, several apertures, a sample

holder and an image recording/viewing system. The objective lens forms a diffraction pattern in the back focal plane with electrons scattered by the sample and gombines them to generate an image in the image plane (1. intermediate image). Thus, diffraction pattern and image are simultaneously present in the TEM. It depends on the intermediate lens which of them appears in the plane of the second intermediate image and magnified by the projective lens on the viewing screen. Switching from real space (image) to reciprocal space (diffraction pattern) is easily achieved by changing the strength of the intermediate lens. In imaging mode, and objective aperture can be inserted in the back focal plane to select one or more beams that contribute to the final image (BF, DF, HRTEM). In selected area electron diffraction (SAED), an aperture in the plane of the first intermediate image defines the region of which the diffraction is obtained.

In the bright field (BF) mode of the TEM, an objective aperture is placed in the back focal plane of the objective lens which allows only the direct beam to pass. In this case, mass-thickness and diffraction contrast contribute to image formation: thick areas, areas in which heavy atoms are enriched, and crystalline areas appear with dark contrast. In spite of the useful information obtainable from BF images, it should be mentioned that the interpretation of contrast is often impeded since these phenomena occur simultaneously.

In dark field (DF) images, one or more diffracted beams are allowed to pass the objective aperture. The direct beam is blocked by the aperture. In contrast to the direct beam, the diffracted beam has interacted strongly with the specimen, and often very useful information is present in DF images, e.g., about planar defects, stacking faults or particle size.

To obtain lattice images, a larger objective aperture has to be selected that allows many beams including the direct beam to pass. The image is formed by the interference of the diffracted beams with the direct beam (phase contrast). If the point resolution of the microscope is sufficiently high and a suitable sample oriented along a zone axis, then high-resolution TEM (HRTEM) images are obtained. In many cases, the atomic structure of the specimen can directly be investigated by HRTEM.

The incident parallel electron wave interacts elastically while passing through the specimen, and the resulting modulations of its phase and amplitude are present in the electron wave leaving the specimen. The wave here, the object exit wave o(r), thus contains the information about the object structure. The objective lens performs

1. The Fourier Transform (Fourier analysis) that creates the diffraction pattern of the object in the back focal plane and 2. the inverse Fourier Transform (Fourier synthesis)

that makes the interference of the diffracted beams back to a real space image in the image plane (lattice image).

2. Energy Dispersive X-ray Spectroscopy & Selected area Electron diffraction

EDS and SAED are two auxiliary function affiliated to SEM/TEM and TEM respectively. Both of them are used to characterize samples based on the constituents and structures. Energy dispersive X-ray spectroscopy (EDS or EDX) is an analytical tool predominantly used for chemical characterization. Being a type of spectroscopy, it relies on the investigation of a sample through interactions between light and matter, analyzing X-rays in its particular case. Its characterization capabilities are due in large part to the fundamental principle that each element of the periodic table has a unique electronic structure and, thus, a unique response to electromagnetic waves. The excess energy of the electron that migrates to an inner shell (in order to fill the newly-created hole) can do more than emit an X-ray. Often, instead of X-ray emission, the excess energy is transferred to a third electron from a further outer shell, prompting its ejection. This ejected species is called an Auger electron, and the method for its analysis is known as Auger Electron Spectroscopy (AES). X-ray Photoelectron Spectroscopy (XPS) is another close relative of EDS, utilizing ejected electrons in a manner similar to that of AES. Information on the quantity and kinetic energy of
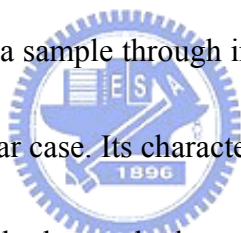
ejected electrons is used to determine the binding energy of these now-liberated electrons, which is element-specific and hence allows chemical characterization of a sample. EDS is often contrasted with its microscale spectroscopic counterpart, WDS (Wavelength-Dispersive X-ray Spectroscopy). WDS differs from EDS in that it uses the diffraction patterns created by light-matter interaction as its raw data.

Selected area Electron diffraction, abbreviated as SAED, is a crystallographic experimental technique that can be performed inside a transmission electron microscope (TEM).

In a TEM, a thin crystalline specimen is subjected to a parallel beam of high-energy electrons. As TEM specimens are typically ~100nm thick, and the electrons typically have an energy of 100-400 kiloelectron volts, the electrons pass through the sample easily. In this case, electrons are treated as wave-like, rather than particle-like (see wave-particle duality). Because the wavelength of high-energy electrons is a fraction of a nanometer, and the spacings between atoms in a solid is only slightly larger, the atoms act as a diffraction grating to the electrons, which are diffracted. That is, some fraction of them will be scattered to particular angles, determined by the crystal structure of the sample, while others continue to pass through the sample without deflection.

As a result, the image on the screen of the TEM will be a series of spots -- the selected area diffraction pattern, SADP, each spot corresponding to a satisfied diffraction condition of the sample's crystal structure. If the sample is moved under the beam, bringing different sections of it under illumination, the arrangement of the spots in the diffraction pattern will change. If the sample is tilted, the same crystal will stay under illumination, but different diffraction conditions will be activated, and different diffraction spots will appear or disappear.

SAD is referred to as "selected" because the user can easily choose which part of the specimen to obtain the diffraction pattern from. Located below the sample holder on the TEM column is a selected area aperture, which can be inserted into the beam path. This is a thin strip of metal that will block the beam. It contains several different sized holes, and can be moved by the user. The effect is to block all of the electron beam except for the small fraction passing through one of the holes; by moving the aperture hole to the section of the sample the user wishes to examine, this particular area is selected by the aperture, and only this section will contribute to the SADP on the screen. This is important, for example, in polycrystalline specimens. If more than one crystal contributes to the SADP, it can be difficult or impossible to analyze. As such, it is useful to select a single crystal for analysis at a time. It may also be useful

to select two crystals at a time, in order to examine the crystallographic orientation between them.

As a diffraction technique, SAED can be used to identify crystal structures and examine crystal defects. It is similar to x-ray diffraction, but unique in that areas as small as several hundred nanometers in size can be examined, whereas x-ray diffraction typically samples areas several centimeters in size.

3.3 Photoluminescence

Photoluminescence, a powerful and breakless analysis technology, can reveal the band structure and the carrier transportation behaviors in a material. Moreover, the doping type, band gap, composition, etc. of the bulk material or the size, path of carrier transportation, lifetime, etc. of the nano-material will be shown in the photoluminescence spectrum.

Photoluminescence is a process in which a chemical compound absorbs photons (electromagnetic radiation), transitioning to a higher electronic energy state, and then radiatives photons back out, returning to a lower energy state. The period between absorption and emission is extremely short, on the order of 10 nanoseconds. Light is directed on a sample, where it is absorbed and imparts excess energy into the material in a process called photo-excitation. The luminescence arising from photo-excitation

is called photoluminescence (PL). The intensity and spectral content of the photoluminescence is a direct measurement of various important material properties. Fig 3.3.1 shows the schematic setup of PL system with He-Cd laser operating at 30mW at the wavelength of 325nm.

Typically, the process of the luminescence consists of three steps, which is (1) excitation, (2) thermal equilibrium and (3) recombination. Through thermal equilibrium, electron-hole pairs (e-h pairs) generated by incident light recombine and create photon. In the energy band gap, impurities and defects form a variety of energy levels, whose corresponding energy produces radiation through radiative recombination and absorption through non-radiative recombination.

3.4 Absorption

If the energy is delivered by incident photons the process is called optical absorption. A number of different phenomena may be associated with the incidence of light on a semiconductor. Fig 3.4.1 shows a schematic of the optical absorption spectrum vs. energy of the photons. For our discussion here, phenomena related to (2) excitons, (3) fundamental absorption processes and (4) impurities are of interest.

For the absorption process the density of states N (E) is of importance, where E is the energy. Due to the uncertainty relation, the volume necessary per state in the momentum space is h^3, where h is Planck's constant. The areas with constant energies

are assumed to be spheres. Hence, considering the spin of the electron, the volume in

the momentum space between E+dE is $2 \times 4\pi p^2 dp$ We write N(E) in the momentum

space as $N(E)dE = \dfrac{8\pi}{h^3} p^2 dp$ From $p = \sqrt{2m^*E}$, it follows

$dp = \sqrt{2m^*} \dfrac{1}{2\sqrt{E}} dE$ and we find $N(E) = \dfrac{(2m^*)^{3/2}}{2\pi^2\hbar^3} \sqrt{E} dE$ with the dimension cm^{-3}

eV^{-1}.

Let us consider now absorption transitions between two direct valleys where all the

momentum-conserving transitions are allowed (see fig 3.4.2), i.e., the transition

probability P_{if} is independent of the photon energy. Every initial state at E_i is

associated with a final state E_f such that $E_f = h\nu - |E_i|$.

Therefore, for parabolic bands, we get

$$h\nu - E_g = \frac{\hbar^2 k^2}{2}\left(\frac{1}{m_e^*} + \frac{1}{m_h^*}\right) \qquad\qquad \text{Eq(3.4.1)}$$

where, the m_e and m_h is the effective mass for electrons and holes, respectively. The

reduced effective mass is

$$m_r = \frac{m_e^* m_h^*}{m_e^* + m_h^*} \qquad\qquad \text{Eq(3.4.2)}$$

Finally, the density of states for a direct transition is given by

$$N(E) = \frac{(2m_r)^{3/2}}{2\pi^2\hbar^3}(h\nu - E_g)^{1/2} \qquad\qquad \text{Eq(3.4.3)}$$

$$n = \int_{E_c}^{\infty} N_e(E)f(E)dE \quad (f(E) = \frac{1}{1 + e^{\frac{E-E_f}{kT}}}) \qquad \text{Eq(3.4.4)}$$

At temperatures of interest, the Fermi function reduces to f (E) ~exp (E$_F$-E/kT) and

we find

$$n = 2\left(\frac{m_e^* kT}{2\pi\hbar^2}\right)^{3/2} \exp\left[\left(E_F - E_c\right)/kT\right]$$ Eq(3.4.5)

and $$p = 2\left(\frac{m_h^* kT}{2\pi\hbar^2}\right)^{3/2} \exp\left[\left(E_v - E_c\right)/kT\right]$$ Eq(3.4.6)

where E_c and E_v mark the energy of the conduction and valence band, respectively.

Although we know the density of states and the carrier contribution, we are not able yet to plot the absorption spectrum of a semiconductor, i.e…, the absorption coefficient as a function of the energy since equation 3.4.3 creates a "severe problem". At hv=Eg, N (E) =0. Theoretically, it is the correct answer but in reality this is always wrong. The density of states is not nil at the band gap of the material. The main reason is the band tails, i.e., a perturbation of the conduction and valence bands by the formation of tails of states extending the bands into the energy gap. An ionized donor exerts an attractive force on the conduction electrons and a repulsive force on the valence holes (acceptors act conversely). Since impurities are distributed randomly in the host crystal, the local interaction will be more or less strong depending on the local crowding of impurities (see fig 3.4.3).

It should be noted that the local energy gap - the separation between the top of the valence band and the bottom of the conduction band is everywhere maintained constant. But the density-of-states distribution, which integrates the number of states

at each energy inside the whole volume shows that there are conduction band states at

relatively low potentials and valence band states in high-potential regions.

The transition between the band tails causes an exponentially increasing absorption

coefficient α (d (lnα) /d (E) =1/kT) and is known as Urbach's rule. The exponential

absorption edge of GaAs was found to correlate quite well with transitions involving

band tails, which can be controlled by doping. Figure 3.4.4 shows the typical

absorption edge of a direct semiconductor.

For the plot of α (E), we write down according to equation 3.4.3

$$\alpha(E)_I = A_0 (E - E_g)^{1/2} \qquad \text{Eq (3.4.6)}$$

and Urbach's rule

$$\alpha(E) = K_0 \exp\left[\frac{\sigma}{kT}\left(E - E_g\right)\right] \qquad \text{Eq(3.4.7)}$$

where A_0 and K_0 are fitting parameter and σ is a phenomenological parameter scaling

the steepness of the absorption edge. The absorption coefficient can be plotted over

energy applying the continuity equations

$$\alpha(E)_I = \alpha(E)_{II} \qquad \text{Eq (3.4.8)}$$

and $\qquad \dfrac{d\alpha(E)_I}{dE} = \dfrac{d\alpha(E)_{II}}{dE} \qquad \text{Eq (3.4.9)}$

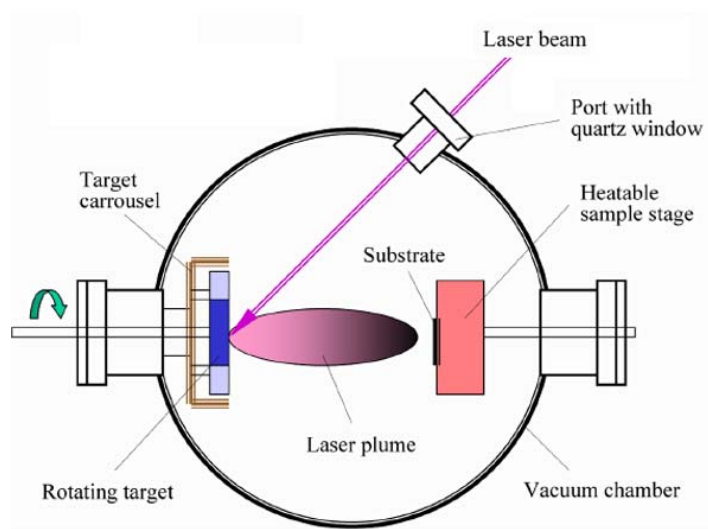We find for cross-over energy between α (E) $_I$ and α (E) $_{II}$,

$$E_{ch} = \frac{kT}{2\sigma} + E_g \qquad \text{Eq (3.4.10)}$$

Therefore, the absorption edge is described by,

$$\alpha(h\nu) = A(h\nu - E_g)^{1/2} \qquad \text{if} \quad h\nu \geq E_{cr} \qquad\qquad \text{Eq (3.4.11)}$$

and $\qquad \alpha(h\nu) = A\sqrt{\frac{kT}{2\sigma}} \exp\left\{\frac{\sigma}{kT}(h\nu - E_\sigma)\right\} \quad \text{if} \quad h\nu \leq E_{cr} \qquad \text{Eq (3.4.12)}$

Schematic of PLD system

Fig 3.1.1 PLD system
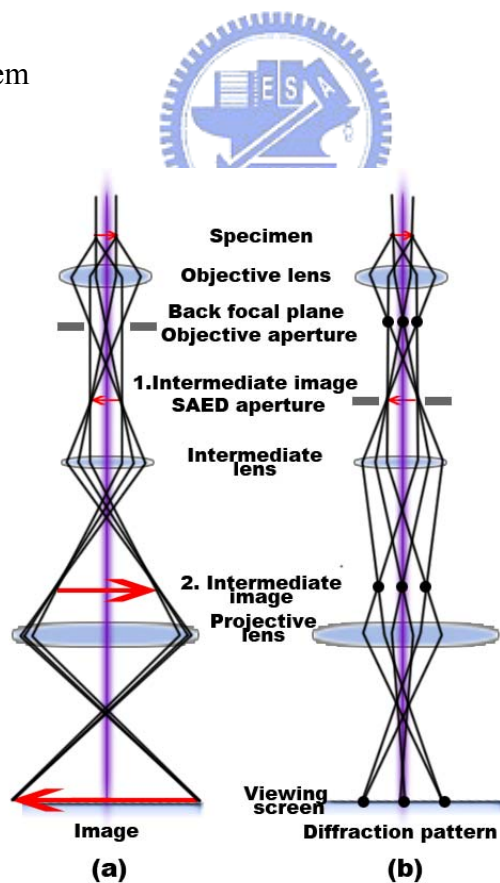

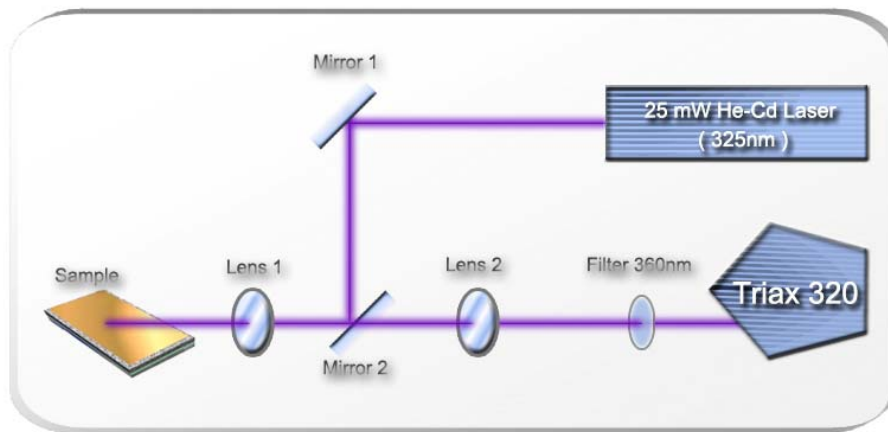Fig. 3.2.1 (a)Ray diagram for viewing the image and (b) the diffraction pattern of the sample.

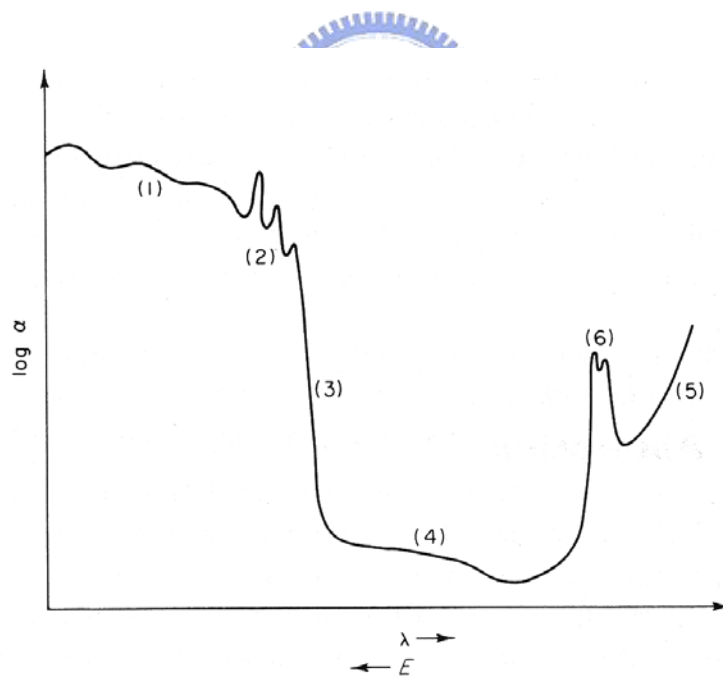Fig 3.3.1 The schematic diagram of photoluminescence setup

Fig 3.4.1 Different types of optical absorption phenomena; (1) transitions of high-lying bands, (2) excitons, (3) fundamental absorption (4) impurity absorption, (5) free-carrier absorption and (6) Reststrahlen absorption
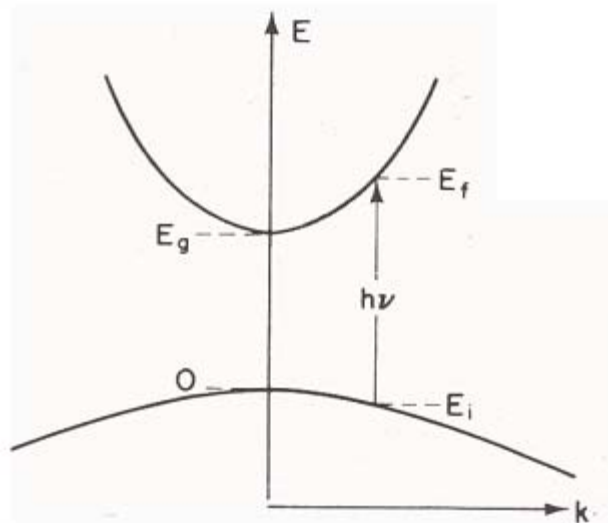
Fig 3.4.2 The momentum-conserving transitions are allowed
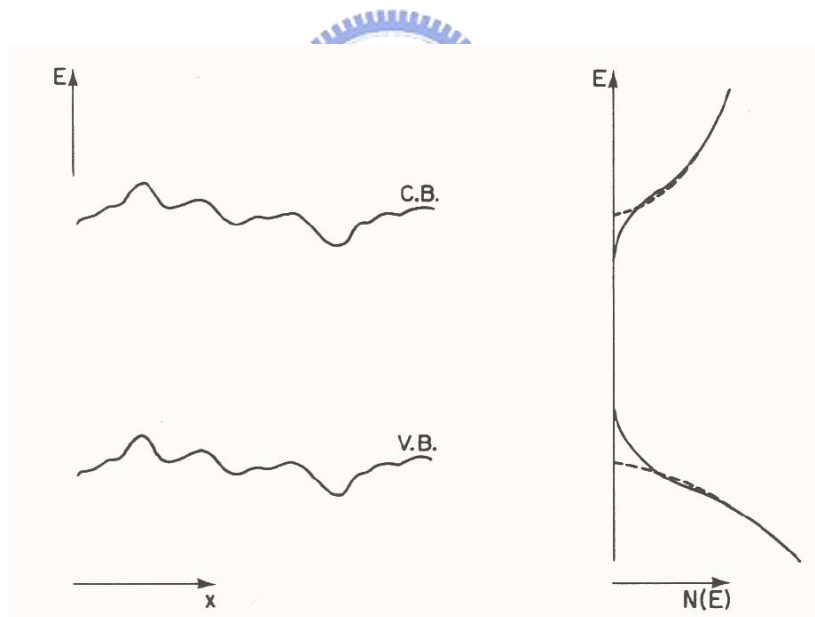

Fig 3.4.3 The left diagram shows the perturbation of the band edges by Coulomb

interaction with inhomogeneously distributed impurities. This leads to the formation

of tails of states shown on the right side. The dashed lines show the distribution of
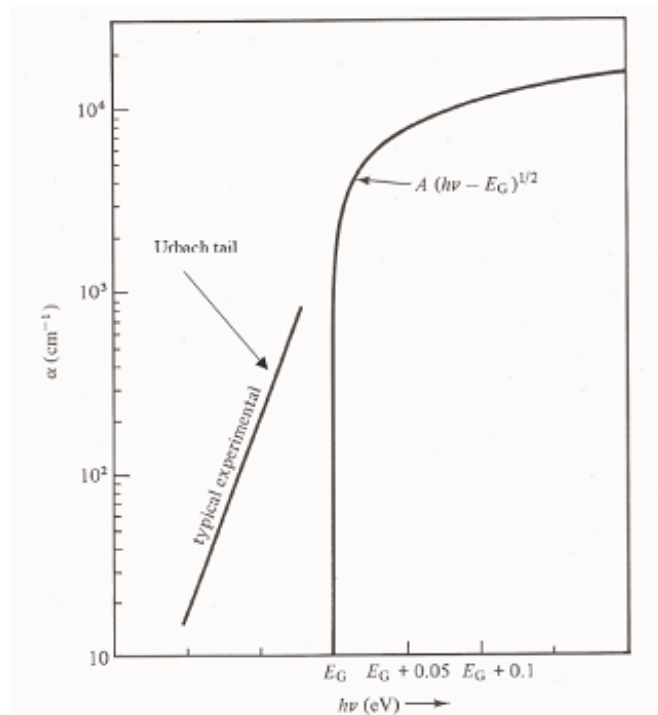
states in the unperturbed case.

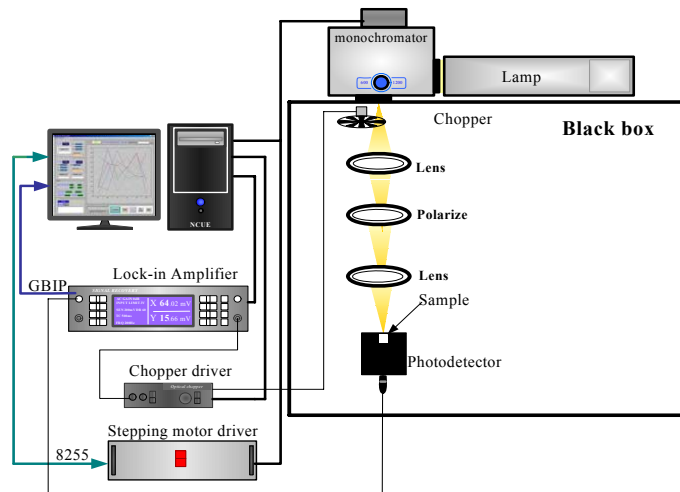Figure 3.4.4 The typical absorption edge of a direct semiconductor.

Fig 3.4.5 Absorption system

Chapter 4 Basic optical characteristics of a-plane ZnO/ZnMgO MQWs

In this chaper, we discuss the basic optical characteristics of a-plane Zno/ZnMgO MQWs. In section 1, we describe the method how we prepare the samples and the growth conditions. In section 2, we discuss the PL spectra of the samples and finite square well model is used to estimate the emission energy of our samples. In section 3, power dependent PL reveals nonpolar ZnO/ZnMgO MQWs is free from QCSE. In section 4, temperature dependent PL shows localization effect is unobvious and the activation energy fitting result shows exciton binding energy enhance by quantum confinement. In section 5, The absorption spectrum was carried out to reveal different recombination paths since the asymmetry strain along c-axis and m-axis which caused valence band splitting. Furthermore, the 92% high polarization of degree of ZnO/ZnMgO MQWs emission was also obtained at 20 K.

4.1 Samples preparation and growth

A KrF excimer laser with λ=248nm was used for PLD deposition of ZnO and ZnMgO films. The base pressure in the growth chamber was 1×10^{-18} Torr. After degreasing in boiled acetone and isopryl alcohol, a 2 inch r-plane sapphire substrate was loaded into the PLD chamber and heated in high vacuum at 850°C for 30 min. Then, the oxygen flow was introduced to the chamber in which the oxygen partial

pressure was then kept at 1.4×10^{-2} Torr for the rest duration of deposition. The targets in the chamber were 2 in pure ZnO and $Zn_{0.8}Mg_{0.2}O$ sintered ceramics. For ZnO film (buffer layer), it was deposited in high vacuum for 5 min at 490°C, and then deposited in oxygen atmosphere at 800°C for 140 min. For five-period $ZnO/Zn_{0.8}Mg_{0.2}O$ film structures, the deposition condition for the first ZnO buffer layer was kept the same as described above, followed by the growth of QWs at 650°C with the thickness of each layer varied by changing the deposition time. $Zn_{0.8}Mg_{0.2}O$ (barrier layer) was deposited for 3 min, and ZnO (well layer) was deposited in vacuum for 1.5 min. Finally, $Zn_{0.8}Mg_{0.2}O$ (capping layer) was deposited for 5min. For ten pairs $ZnO/Zn_{0.8}Mg_{0.2}O$ MQWs growth, ZnO film (buffer layer) was deposited in high vacuum for 2 min at 750°C, and then deposited in oxygen atmosphere at 750°C for 40 min, and $Zn_{0.8}Mg_{0.2}O$ (buffer layer) was deposited at 750°C for 31 min. ZnO (well layer) was deposited at 750°C for 40 sec, and $Zn_{0.8}Mg_{0.2}O$ (barrier layer) was deposited at 750°C for 70 sec. Micro-structural characterization was carried out using cross-sectional transmission electron microscopy (TEM) in the Fig. 4.1.1 (a) (b) 4.1.2 (a) (b). The X-ray energy-dispersive spectroscopy confirmed that the Mg composition of the quantum well is around 20%. For the five pairs $ZnO/Zn_{0.8}Mg_{0.2}O$ MQWs, ZnO buffer layer is around 300nm thick, the $Zn0_{0.8}Mg_{0.2}O$ barrier width is around 8.3 nm thick, and the ZnO well width is around 5.6 nm thick. As for the ten pairs ZnO

/$Zn_{0.8}Mg_{0.2}O$ MQWs growth, ZnO buffer layer is around 300nm thick, $Zn_{0.8}Mg_{0.2}O$

buffer layer is around 100nm, the $Zn0_{0.8}Mg_{0.2}O$ barrier width is around 2.3 nm thick,

and the ZnO well width is around 1.8 nm thick. The selected area diffraction (SAD)

pattern shown in Fig. 4.1.3 (a) (b) is obtained from the interface between the ZnO

layer and sapphire substrate where electron beam is from c-axis (m-axis) in Fig

4.1.3(a) (Fig. 4.1.3 (b)). The crystal plane of (1-100) ZnO parallels to (11-20) sapphire

and (000-1) ZnO parallels to (1-10-1) sapphire.

4-2 Photoluminescence spectra of a-plane ZnO/ ZnMgO MQWs

Low temperature PL measurements were performed using the cw 325 nm He–Cd

laser operating at an excitation level of 25 mW. Fig. 4.2.1 shows the PL spectra of

a-plane ZnO /$Zn_{0.8}Mg_{0.2}O$ MQWs at 20K. The peak energy of film a-plane ZnO film

is at 3.375eV which is slightly larger than c-plane ZnO film (~3.36eV) .The peak

energy of five pairs ZnO/$Zn_{0.8}Mg_{0.2}O$ MQWs is about 3.407eV which is blue shift

about 32meV. The paek energy of ten pairs ZnO/$Zn_{0.8}Mg_{0.2}O$ MQWs is about

3.538eV which is blue shift about 163meV. The PL spectra also display the emission

from the buffer layer which is around 3.37eV (D^0X) and 3.318eV (e-A_0) in all

samples. [30].

Room temperature PL was also performed in the Fig 4.2.2 (a) (b). Finite-squqre

well model was used to calculate the peak energy of the five & ten pairs

ZnO/Zn$_{0.8}$Mg$_{0.2}$O MQWs that takes into account the exciton binding energy. The exciton energy in the QW is calculated by Eq(4.2.1).

$$E_{ex}^{QW} = E_g^{ZnO} + \Delta E_e + \Delta E_h - E_b^{QW}$$
Eq(4.2.1)

E_g^{ZnO} is the band gap energy of ZnO, $\triangle E_e$ and $\triangle E_h$ are the confinement energies of electrons and holes, respectively, E_b^{QW} is the exciton binding energy in QWs. E_g^{ZnO} is 3.37eV[31] and the exciton binding energy is about 60meV. Because the PL spectra of five pairs ZnO/Zn$_{0.8}$Mg$_{0.2}$O MQWs includes the emission of QWs and buffer ZnO, the peak energy was fitted by lorentzian waveform. The effective mass of electron is 0.28m$_0$ and the effective of hole is 0.58m$_0$ (m$_0$ is electron mass) The band-offset ratio is 60:40. The energy of Zn$_x$Mg$_{(1-x)}$O is calculated by Eq(4.2.2). [32][33]

Zn$_x$Mg$_{(1-x)}$O=3.37+2.51x(eV)……………………… Eq(4.2.2)

For five pairs ZnO/ZnMgO MQWs, the calculation result was 3.35eV. For ten pairs ZnO/ZnMgO MQWs, the calculation result was 3.506eV. The slight different may casue from the enhancement of exciton binding energy, the single quantum well approach…..etc.

4.3 Nonpolar characteristics of a-plane ZnO/ ZnMgO MQWs

In c-plane polar structure, the built-in field with the MQWs would lead to band tilting. If the photo-genarated carriers were injected into the MQWs, the built-in electric field could be screened and result in a blue-shift of PL energy peak

[34]. As we mentioned above, the useful approach for reducing the built-in electric field is to grown MQWs along the nonpolar direction. In this section, we performed the power dependent photoluminescence to realize the built-in field influence on our samples.

The power dependent photoluminescence was demonstrated by using He-Cd laser operated at 325 nm. The excitation power increased from 0.05 to 35 mW. Fig.4.3.1 (a) (b) showed the PL spectra as a function of excitation power for our samples at low temperature. *Morhain C et al* had calculated the built-in electric field in polar ZnO/ZnMgO MQWs and his experiment result showed when power density vary from 0.1 mW/cm^2 to 100W/cm^2 the PL spectra was under large blue–shift(~80meV). Fig 4.3.2(a) (b) showed power-dependent PL results, which exhibited the un-shifted peaks in a-plane ZnO/Zn$_{0.8}$Mg$_{0.2}$O MQWs as increasing pumping power density. It is well known for a-plane hexagonal MQW with the non-polar characteristic and the flat-band structure demonstrates that the structure possesses free electric field. We also analyzed different power dependences I~P$^\alpha$ for a-plane ZnO/Zn$_{0.8}$Mg$_{0.2}$O MQWs where I is the integrated PL intensity, P is the excitation power density, and α is the power index. α value is around 1. We exclude out the influence non-recombination which also imply no built-in electric field in this structure in terms of our fitting result.

4.4 The localization effect of a-plane ZnO/ZnMgO MQWs

In order to further understand whether the localization effect plays an important role in nonpolar ZnO MQWs or not, the PL spectra were measured under different temperature in the range of 20K to 300K using the CW 325 nm He–Cd laser.

Fig. 4.4.1 (a) (b) shows the evolution of PL spectra as a function of temperature for the a-plane ZnO/ZnMgO MQWs. The decrease of PL intensity with increasing temperature is observed. Thermal quenching PL intensity with increasing temperature is a general phenomenon in semiconductor nanostructure which is caused by carriers thermalization from the radiative recombination centers or/and localized states to the nonradiative recombination centers or/and delocalized states. This thermal quenching behavior will be discussed later.

The emission from the buffer layer is strong at low temperature (~20K), but as the temperature got raised the emission from quantum well will dominate the PL spectra. This is evidence that excitons are confined in quantum well, because the thermal quenching in quantum well is smaller than in buffer layer. In order to check the situation of alloy and interface fluctuations in our samples, we further analyze the peak shift of ZnO/ZnMgO MQWs emission over the investigation temperature range. The result is shown in Fig. 4.4.2 (a) (b). In our samples, the emission energy decreases monotonically with increasing temperature. We didn't observe the exciton

localization effect [35] [36] which may induce red-blue-red shift(S-curve) of peak

energy with increasing temperature. It seems no deep localization states in the

ZnO/ZnMgO MQWs system. In InGaN/GaN MQWs system, S-curve is a very

common phenomenon. Inhomogeneity due to interface fluctuation, InN/GaN

segregation, and the band tail states originating from the high density of defects are

responsible for the so-called S-shaped temperature dependent behavior in the

InGaN/GaN MQWs. Whereas there is no this relevant problems with well material of

ZnO so that ZnO/ZnMgO MQWs is more stable and the localization center is more

uniform in comparison to InGaN/GaN MQWs.

Figure 4.4.3 show the Arrhenius plot of the normalized integrated PL intensity for

the a-plane Zno/ZnMgO MQWs emission from MQWs over the temperature range

under investigation. The intensity reduction is remarkable, the degree of PL intensity

reduction from 20K to 300K is more severe when the well width gets thicker which

indicates a higher PL efficiency in the thinner well width samples [35]. We use the

equation below to get a good fit to our experimental data of the activation energy in

thermally activated processes [37].

$$I(T) = I_0 / [1 + a*\exp(-E_a/K_BT) + b*\exp(-E_b/K_BT)] \qquad \text{Eq. (4.4.1)}$$

Where $I(T)$ is the temperature dependent integrated PL intensity, I_0 is the integrated

PL intensity at 20K, K_B is the Boltzmann's constant, a and b are the rate constants,

and E_a and E_b are activation energy for two different non-radiative channels. This suggests that there are two non-radiative paths exist at the same time which one of them dominates in the low temperature region and the other dominate in the high temperature region.[38]

Since the activation energy we get from our samples is much less than the bandgap energy difference between the well and the barrier. It is impossible to account the thermal quenching of ZnO MQWs emission for carriers thermalized from the ZnO wells to the ZnMgO barriers. Therefore, the more reasonable explanation for the quenching of luminescence is that increasing temperature increases the probability of excitons to be trapped by nonradiative recombination centers within the well at the same time when carriers are activated out of the loacalization minima of potential fluctuation which may be caused by compositional、interface fluctuation. Or the excitons partly dissolve into free carrier which may be trapped by nonradiative recombination centers. The smaller activation energy was attributed to the shallow localization states forming in the interface fluctuation of well and barrier layer. The larger activation energy was attributed to the enhancement of the exciton binding energy [39]. *Giuliano Coli et al* had calculated the enhancement of the exciton binding energy due to quantum confine effect [40]. As temperature rose, excitons partly dissolved into free carriers which may decrease the

efficiency of excitons recombination. Furthermore, the free carriers may be trapped by non-radiative centers which also decrease the emission intensity. In our fitting result, the enhancement of binding energy is larger in thin ZnO/ZnMgO MQWs.

4.5 In-plane polarization effect of a-plane ZnO/ ZnMgO MQWs emission

4.5.1 In-plane polarization effect of a-plane ZnO/ ZnMgO MQWs emission

It was mentioned in section 2.3 that due to the inherent lower symmetry of non-polar heterostructure, a-plane ZnO/ZnMgO MQWs is likely to experience anisotropic in-plane strain. A PL measurement was carried out at low temperature using the CW 325nm He-Cd laser and a visible polarizer was set in front of the spectrometer to examine the polarization property of our samples. In the case, of the a-plane ZnO/ZnMgO MQWs, an angle of $90°$ is defined to be perpendicular to the c [0001] axis ($E \perp C$) while the $0°$ is along m [1-100] axis ($E \parallel C$). Fig 4.5.1 (a) (b) display the polarization–dependent PL spectra of our samples for polarization angles between 0° and 90° in steps of 15°. The value of polarization degree ρ is defined as

$$\rho = (I_\perp - I_\parallel) / (I_\perp + I_\parallel) \qquad \text{Eq. (4.5.1)}$$

, where $I_\perp$ and $I_\parallel$ are PL intensities for $E \perp C$ and $E \parallel C$. Fig 4.5.2 (a) (b) showed the pretty symmetric of the normalized PL intensity versus the in-plane polarization angle. The polarization degree ρ of our samples are 92%、84.8% for five pairs MQWs and ten pairs MQWs, respectively. This high polarization ration phenomenon was

observed in a-plane ZnO thin film on r-plane sapphire, too [41]. However, we wanted

to analyze the energy level of our samples. Polarized absorption spectra was used to

measure the electronic band structure(EBS) modification of ZnO/ZnMgO MQWs

grown along (11-20) orientation due to biaxial, anisotropic in-plane strain.

4.5.2 Polarized absorption spectra of a-plane ZnO/ZnMgO MQWs

Low temperature polarized absorption spectra measurements were performed using

the Xe lamp as white light source. We use two different polarized lights (along c-axis

and along m-axis) to pass through the five pairs MQWs which has higher polarization

ratio. Chopper and look-in amplifier was used to amplify our signals.

$$I(l) = I_0 e^{-\alpha l} \rightarrow \alpha(h\upsilon) \, l = \ln[I_0/I(l)] \quad \alpha(h\upsilon) \sim A(h\upsilon - E_g)^{1/2} \rightarrow \quad \alpha(h\upsilon) \, l \sim A(h\upsilon - E_g)^{1/2} l$$

$$[\alpha(h\upsilon) \, l]^2 \sim A^2(h\upsilon - E_g)l^2 \sim \{\ln[I_0/I(l)]\}^2 \qquad\qquad Eq4.5.2$$

I_0 was background white light source. $I(l)$ was the signal which transmits from the

sample. Fig 4.5.3 showed the measurement result and fig 4.5.4 showed a simple

electronic band structure. We can clearly recognize two different absorption spectra

which are attributed two different energy levels. We identified four distinct band-edge

transitions at 3.385eV, 3.429eV, 3.474eV, 3.5219eV. They were identified as E1 and

E2 excitons in ZnO buffer layer [41], E1 and E2 excitons in ZnO/ZnMgO MQWs.

The E1 exciton (lowest energy) was mainly polarized to $E \perp C$, and weakly polarized

to $E \parallel C$. The E2 exciton (next higher energy) was exclusively polarized to $E \parallel C$.

However, the peak at 3.474eV, 3.5219eV were not observed in the PL spectra. Because the emission of ZnO at low temperature was dominated by donor bound excitons, it was difficult to observe the E1 or E2 emission. The energy difference between E1 and E2 was the main reason which induced high polarization ratio. We assumed $\triangle E = E2-E1$. For buffer ZnO layer, $\triangle E$ was about 44meV which was larger than ref [41] For ZnO MQWs, $\triangle E$ was about 45meV. The $\triangle E$ was larger then 25meV, but ρ decreased to 0.68 at room temperature. There are other factors which may influence the degree of polarization. We couldn't give a clear explanation for such result now, a full understanding of the degree of polarization of these nonpolar samples will probably emerge only after considerable further study.

4.6 Conclusion

In conclusion, a-plane ZnO/ZnMgO MQWs of different well width grown by PLD on r-plane sapphire were investigated. However, the quantum confinement decreases as the quantum well width increased. Temperature dependent PL clearly show excitons confined in quantum well. From the fitting result of activation energy, the exciton binding energy was further enhanced by quantum well. No built-in electric field was observed in the power dependent PL measurement for all samples. High degree polarization ratio (92%) was observed in ZnO/$Zn_{0.8}Mg_{0.2}$O MQWs (@20K). From the polarized absorption spectra experiment results, the electronic band

structure was observed. Large $\triangle E$ (E2-E1) was the main reason which induced high
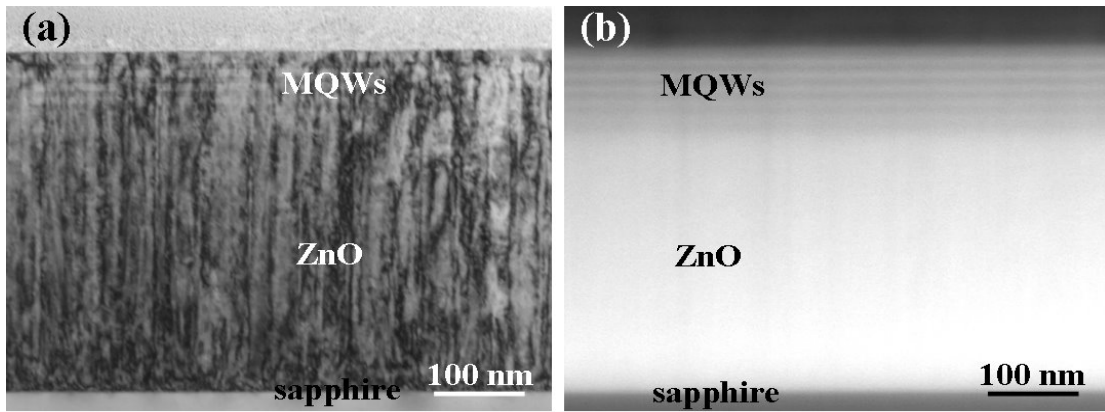
polarization ratio.

Fig. 4.1.1 TEM measurement results of the five pairs ZnO/ZnMgO MQWs (a) bright
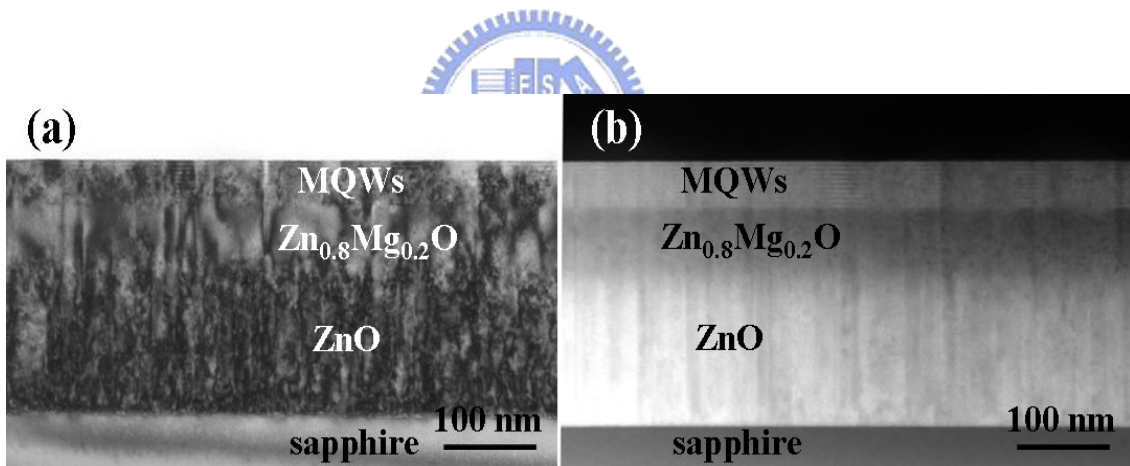
field (b) dark field

Fig. 4.1.2 TEM measurement results of the ten pairs ZnO/ZnMgO MQWs (a) bright
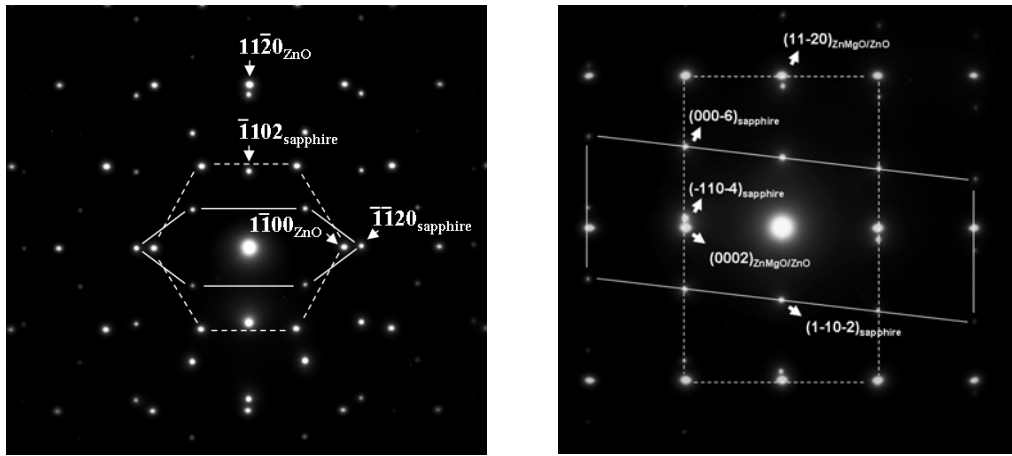
field (b) dark field

Fig. 4.1.3 Selected area Electron diffraction (a) Electron beam direction from c-axis
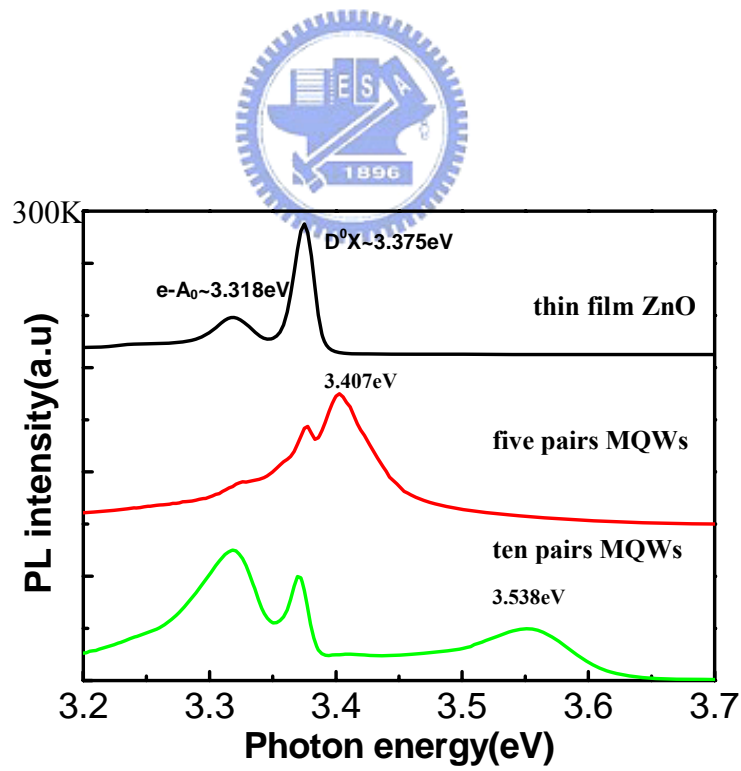
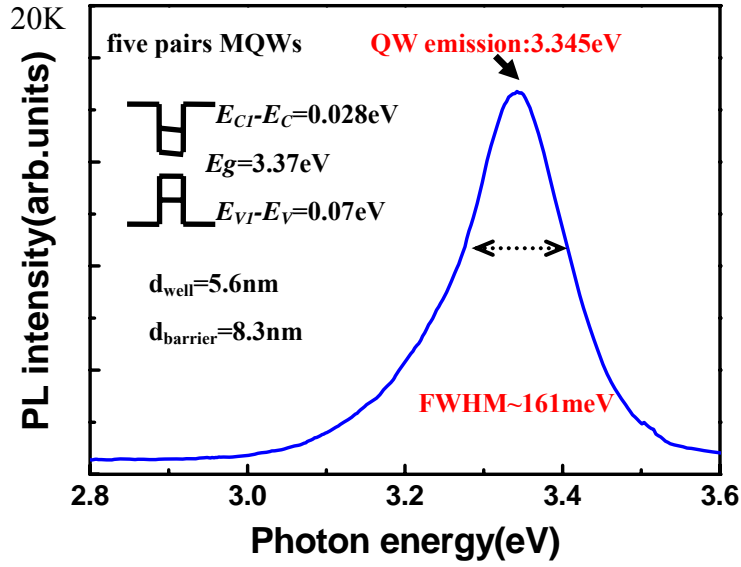(b) Electron beam direction from m-axis

Fig.4.2.1 The PL measurement results of all samples at 20K.

Fig 4.2.2(a) Simulation & PL spectrum of five pairs ZnO/ZnMgO MQWs (@300K)
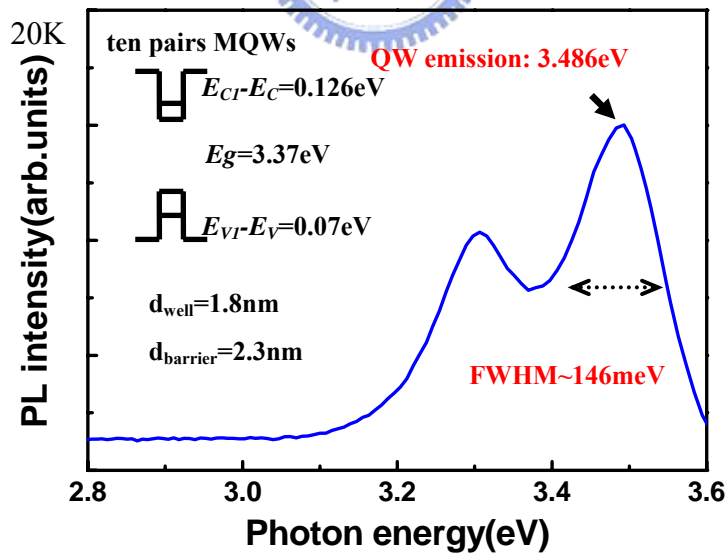
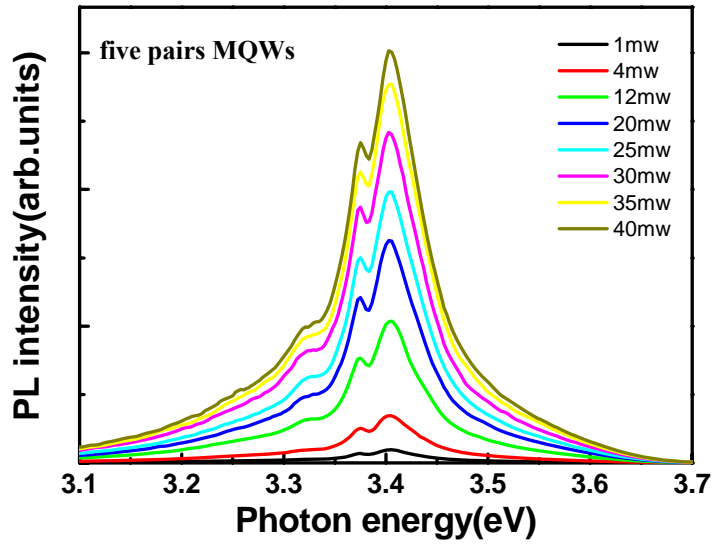Fig 4.2.2(b) Simulation & PL spectrum of ten pairs ZnO/ZnMgO MQWs (@300K)

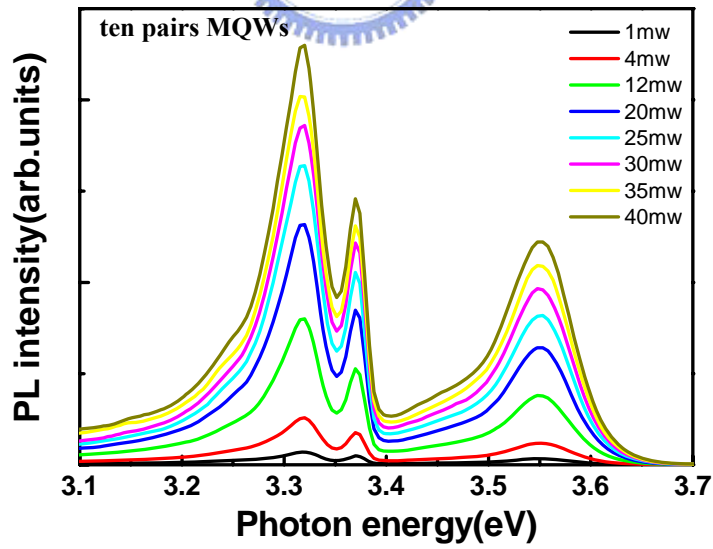Fig 4.3.1 (a)Power-dependent PL spectra for five pairs ZnO/ZnMgO MQWs.

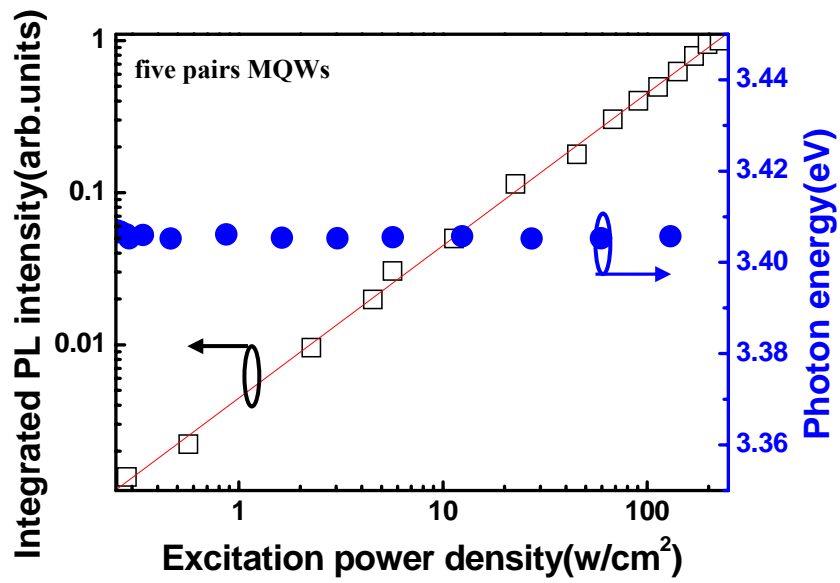Fig 4.3.1 (b)Power-dependent PL spectra for ten pairs ZnO/ZnMgO MQWs.

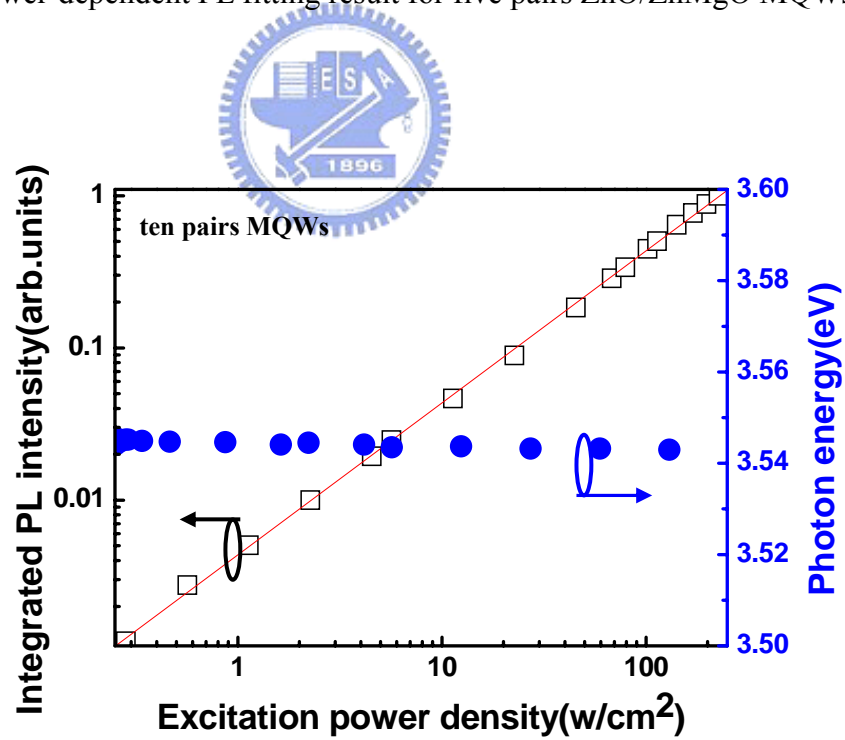Fig4.3.2 (a) Power-dependent PL fitting result for five pairs ZnO/ZnMgO MQWs.

Fig4.3.2 (b) Power-dependent PL fitting result for ten pairs ZnO/ZnMgO MQWs.
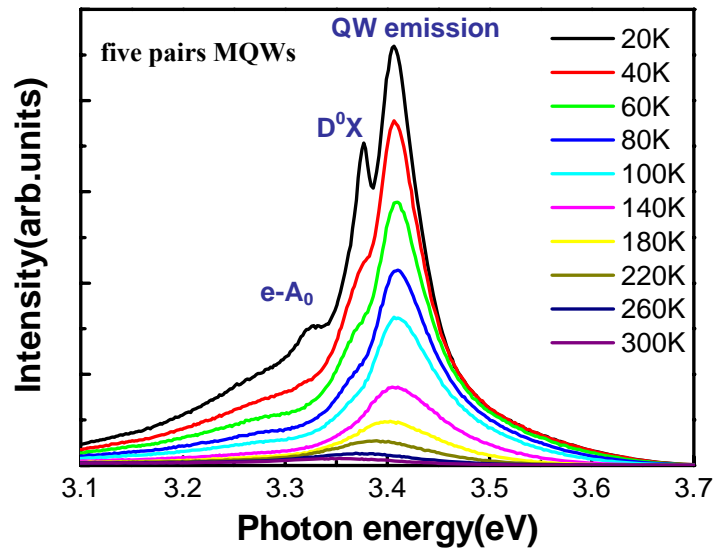
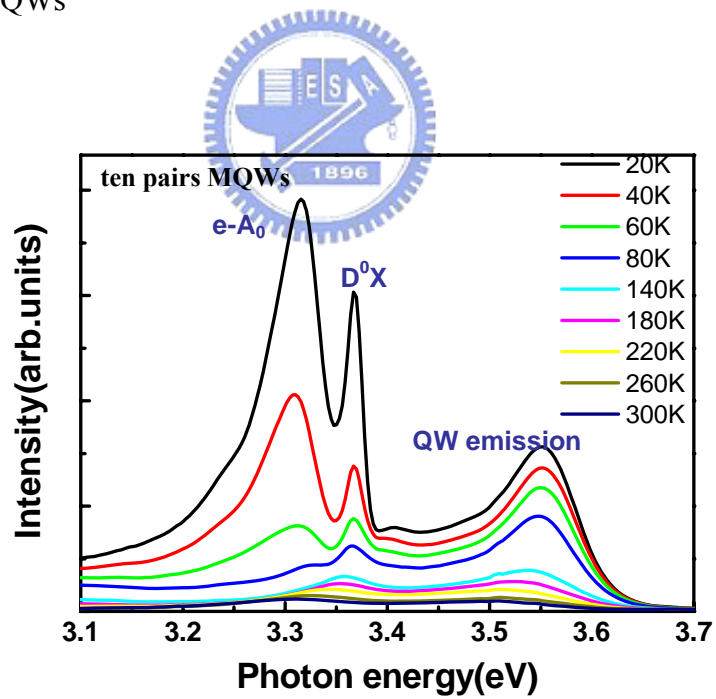Fig 4.4.1 (a)The evolution of PL spectra as a function of temperature for the five pairs ZnO/ZnMgO MQWs

Fig 4.4.1 (b)The evolution of PL spectra as a function of temperature for the ten pairs

ZnO/ZnMgO MQWs
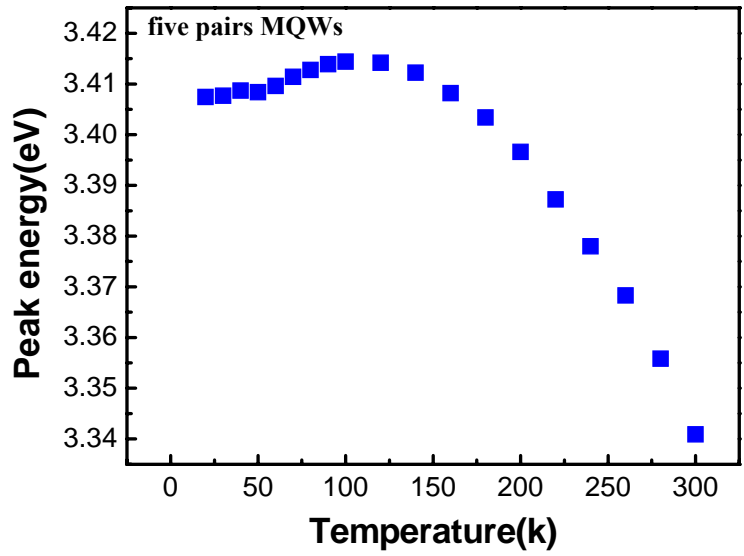
Fig 4.4.2(a)The peak shift of five pairs ZnO/ZnMgO MQWs emission over the

investigation temperature range.

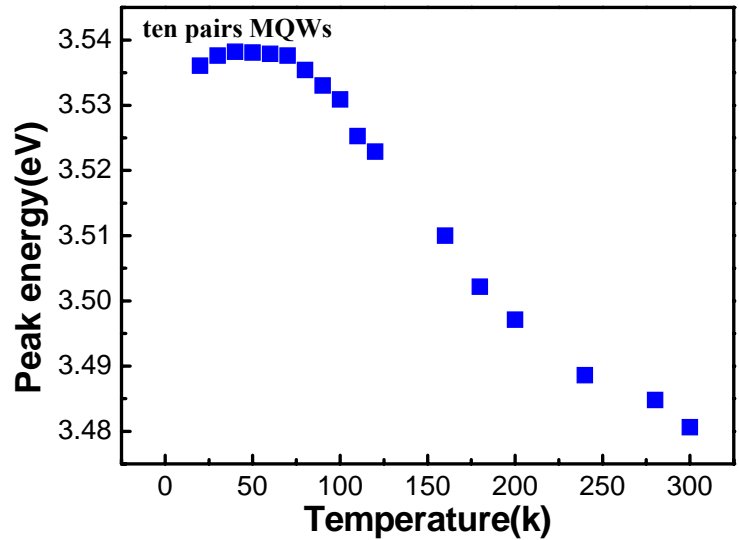Fig 4.4.2(a)The peak shift of ten pairs ZnO/ZnMgO MQWs emission over the

investigation temperature range.
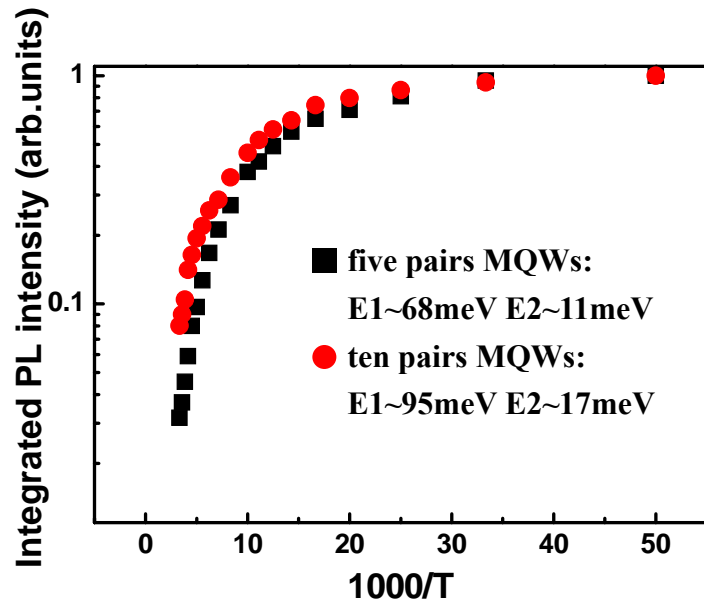
Fig 4.4.3 The Arrhenius plot of the normalized integrated PL intensity for the a-plane

Zno/ZnMgO MQWs emission from MQWs over the temperature range under

investigation.

Fig 4.5.1(a) The polarization–dependent PL spectra of five pairs MQWs for

polarization angles between 0° and 90° in steps of 15°
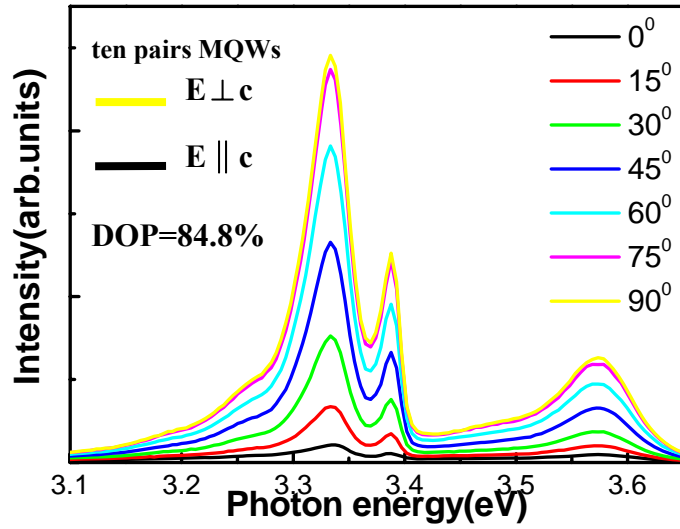
Fig 4.5.1(b) The polarization–dependent PL spectra of ten pairs MQWs for

polarization angles between 0° and 90° in steps of 15°
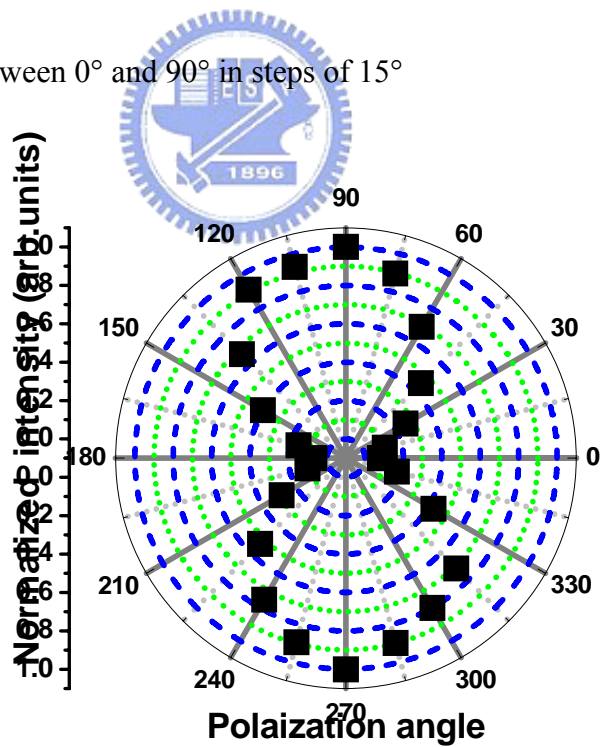
Fig 4.5.2 (a) The pretty symmetric of the normalized PL intensity versus the in-plane

polarization angle.

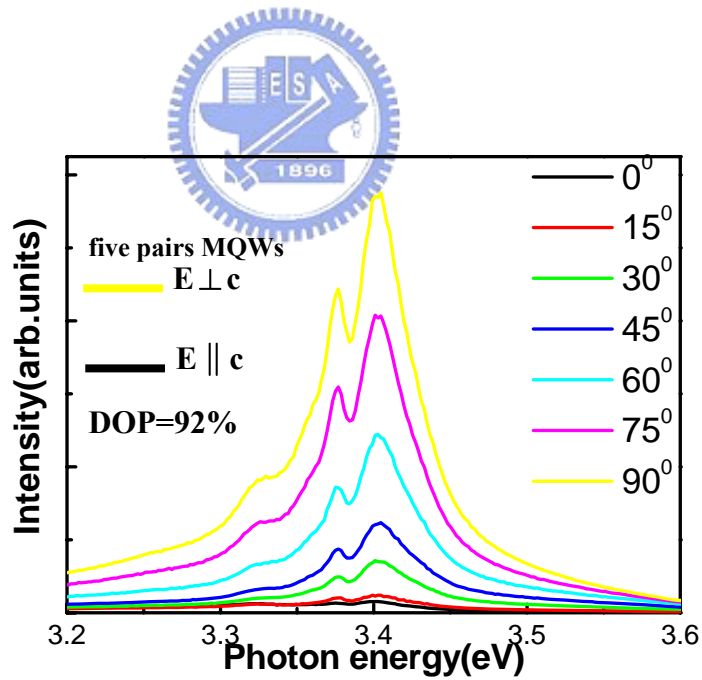Fig 4.5.2 (b) The pretty symmetric of the normalized PL intensity versus the in-plane

polarization angle.

Fig4.5.3 Polarized absorption spectrum of five pairs ZnO/ZnMgO MQWs.

Conduction-band edge

$E \parallel (0001)$ $E \perp (0001)$

E1

E2

Fig4.5.4 A simple graph of electronic band structure

Chapter 5　　Random lasing behavior of a-plane ZnO/ZnMgO MQWs

5.1 Introduction

If we increase the densities of excitons and/or free carriers in a semiconductor, e.g. by excitation with short and intense laser pulses or by carrier injection in a forward-biased p (i) n-junction some phenomena will appear in the spectra.
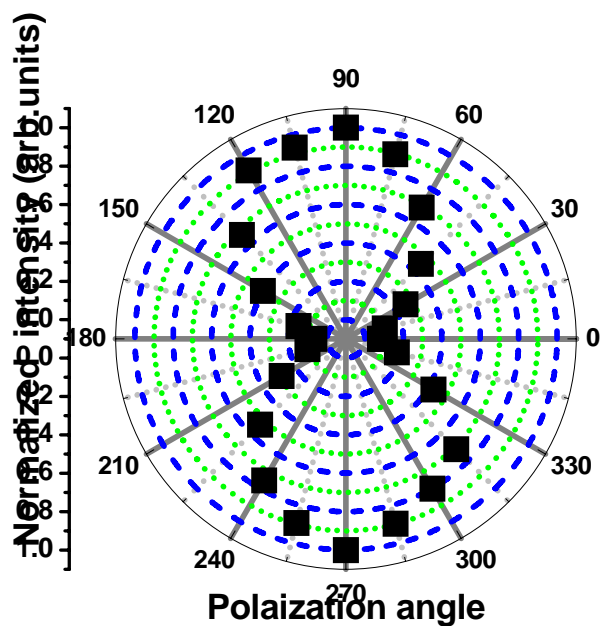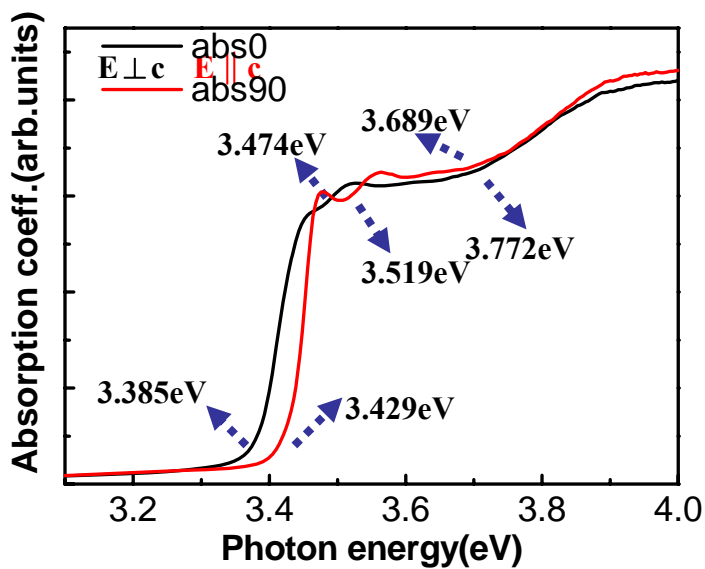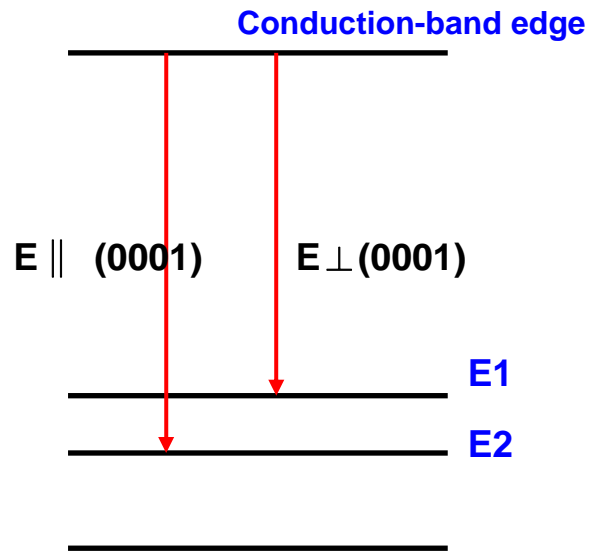
In Fig. 5.2 [42] we displayed a simple graph and the processes that occur with increasing excitation intensity. In the low-density limit there are free excitons, at low temperature also bound-exciton complexes and at higher temperatures also some free carriers resulting from either the thermal ionization of excitons or from donors, since undoped ZnO is usually n-type.

At middle densities we enter the region of nonlinear optics with another emission processes. The middle density region is ideally considered that excitons are still good quasiparticles. If two excitons meet during their lifetime on their diffusive path through the sample, different emission can occur. They can scatter elastically under conservation of momentum and kinetic energy resulting in a density-dependent increase of their homogeneous line width. They can scatter inelastically. In this situation one exciton is scattered into a higher state with $n_B = 2, 3, . . .$ or into the continuum state, while the other is scattered down on the photon-like part of the

dispersion relation again under energy and momentum conservation, leaving the sample as a luminescence photon. The emission bands are broadened due to this thermal distribution of excitons in their bands in addition to homogeneous broadening and are known as P_2 or P_∞ bands. See Fig. 5.3 for a schematic drawing of the inelastic exciton–exciton scattering (X–X) process and its observation. Other semiconductors also have the X–X process [43] for ZnO see, e.g. [44, 45]. Energy and momentum conservation relation is as below eqution.

$$\hbar\omega_{Pn} = E_x(n_B = 1, k = 0) - E_x^b \left(1 - \frac{1}{n_{Bf}^2} \right) - \frac{\hbar^2}{M} k_{i1} k_{i2} \qquad \text{Eq5.1}$$

Where E_x on the rhs gives the exciton ground state $M = m_e + m_h$ is the translational exciton mass and the k_{i1} and k_{i2} are the wavevectors of the two excitons in the initial state. The thermal average of the last term on the rhs of Eq. 5.1 can be approximated by $3\delta\,k_B T$ with $0 < \delta < 1$.

At the highest densities the excitons can not exist as individual quasiparticles and a new collective phase of still Coulomb-correlated electrons and holes is formed, the so-called electron–hole plasma (EHP). See Fig. 5.2. The transition from an insulating gas of neutral excitons to the metallic state of an EHP is also known as a Mott transition occurring at the Mott density n_M. In direct gap materials the transition is generally smooth and not abrupt [46]. The calculation in Fig. 5.4[42] shows as a function of the electron–hole pair density n_P the renormalization of the gap, the

chemical potential of the e–h pair system and the exciton energy at $-1R_y$. The energies are given in units of the excitonic Rydberg or binding energy $R^*_y = E_b^x$. The calculation result is for CdS. The results are similar for ZnO, but n_M is rather at $n_p = 3$ to 5×10^{17} cm^{-3} instead of 8×10^{16} cm^{-3} [46] See below for the deduction of the numbers for ZnO. The many-particle effects will induce the bandgap renormalization (BGR) phenomenon. The width of the forbidden gap monotonously decreases with increasing electron–hole pair density n_P, due to exchange and correlation effects. The binding energy of the exciton E_b^x (n_P) also decreases with increasing n_P, because the Coulomb attraction of electron and hole is increasingly screened by the additional electron–hole pairs and vanishes at n_M. As a consequence the absolute energy of the exciton $E_x = E_g(n_P) - E_b^x$ (n_P) is almost constant but its damping increases with n_P. In ZnO the n_M is around 3 to 5×10^{17} cm^{-3}, and is only weakly dependent on temperature. The increasing redshift of the emission with increasing excitation reflects the decrease of $E_g^{'}$ with increasing n_P and the narrowing of the emission band indicates the onset of stimulated emission.

Figure 5.1 shows the optical pumping scheme for our ZnO/ZnMgO MQWs. The optical pumping of the samples was performed using a frequency-tripled Nd: YVO4 355-nm pulsed laser with a pulse width of 0.5 ns at a repetition rate of 1 kHz. The pumping laser beam with a spot size about 50μm ×130μm was incident obliquely 60°

to the sample surface. The light emission from the sample was collected using an imaging optic into a spectrometer/cooling charged coupled device (Jobin-Yvon Triax 320 Spectrometer) with a spectral resolution of 0.1nm.

5.2 Optical pumping of a-plane ZnO/ ZnMgO MQWs

At high excitation intensity ($\sim$55.7MWcm^{-2}), many sharp peaks emerge on the spectra (Fig5.5). The FWHM of each individual peaks was about 0.37nm and the mode spacing was about 0.65nm. In order to figure out this phenomenon, from low to high pumping density was used to observe the PL spectra.

Fig 5.6 clearly displayed various spectra under different pumping intensity. At 3.9MWcm^{-2} pumping density, the PL spectrum was as similar as the previous measurement result. We named this emission mechanism as spontaneous emission and the peak energy was around 3.313eV. At higher ($\sim$31.3MWcm^{-2}) pumping density, another peak emerges at the lower shoulder of the spontaneous emission which has peak energy around 3.22eV. This behavior was mentioned above as ZnO P-band emission which was induced by exciton-exciton scattering. As the excitation density further increasing, the EHP band emission appeared at around 3.139eV. The peak energy of EHP band is lower than P band emission. This is due to the excitons density exceeded the Mott density, the excitons can not exist as individual quasiparticles. Then, electron–hole plasma was formed under this condition. From ref [47], we get

the relation between spontaneous emission and P band emission.

$$P_n = E_{ex} - E_b^{ex}(1-\frac{1}{n^2}) - \frac{3}{2}kT(n=2,3,4........\infty)\ldots Eq5.2$$

We can use Eq5.2 to obtain the exciton binding energy which is about 66meV. This

result is close to the previous fitting result. There are many individual peaks in the

EHP band emission. We presumed the random lasing behavior of a-plane

ZnO/ZnMgO MQWs was observed. Random laser represented a laser amplifier due to

random scattering mechanism, as opposed to the reflective feedback by the mirrors, so

we also called the random laser as a mirrorless laser. In the late 1990s, random lasers

with coherent feedback were realized with disordered semiconductor and organic

materials [48]. The interference of waves produces the amplitude feedback. In the

active medium of a random laser, light is scattered by some disorder and a random

trip is achieved before leaving the active medium. A photon may generate the

stimulated emission of a second photon as it travels through a gain medium. There are

characteristics length scales. We use it to describe the action of photon in the medium.

The gain length is the distance a photon travels before generating a second photon.

The average length is that a photon travels in the gain medium. With the number of

scattering centers increase, the average path length of photons increases. When it is

equal to the gain length, each photon will induce another photon before leaving the

medium. This situation has been called lasing without coherent feedback. When

scattering gets stronger, after multiple scattering light may return to the scattering

center from which it was scattered before. A closed-loop path for light is formed.

When the gain along the loop reaches the loss, lasing oscillation occurs in this closed

loop which forms a cavity. Their phase relationship determines the lasing frequencies.

The feedback is provided by the disorder-induced scattering. In ZnO system, this

behavior was extensively observed. For example, Z. K. Tang et al [49] had discovered

ultraviolet laser emission from self-assembled Zno microcrystallite thin films at

room-temperature. H. GaO et al [48] had observed ultraviolet lasing formed by

scattering in semiconductor polycrystalline films. S. F. Yu et al [50] also discovered

the random laser action in ZnO nanorod arrays in ZnO epilayers.

Fig 5.7 shows the optical pumping result. At low excitation density, single-broad

emission spectra with a FWHM of around 20nm were observed. When excitation

intensity increased; many individual peaks appeared on the spectra. The FWHM of

each individual peaks was about 0.37nm. The mode spacing roughly equated to

0.65nm. A further increase in pump intensity increases the number of lasing modes as

the increase in optical gain excites more cavity modes with higher losses. The central

position of lasing peak energy was gradual red-shift, when excitation intensity

increased. This is so called bandgap renormalization (BGR) phenomenon. This

phenomenon is a characteristic of EHP lasing behavior. We further fitted the lasing

threshold. The lasing threshold was about 47.33MWcm^{-2}. Fig 5.9 shows the evolution of the emission spectra when the excitation area was varied at a fixed pump intensity. When the excitation area was increased, more lasing peaks emerged in the emission spectra. This is because in a large excitation area, more closed-loop paths for light can be formed. As a result, random laser action could occur in more cavities formed by recurrent scattering. On the other hand, when the excitation area was reduced to below a critical size, laser oscillation stopped. This is because if the closed-loop paths are too short, the amplification along the loop was not high enough achieve lasing. A major advantage of random lasers over regular lasers is that their production is cheap and the required technology relatively simple. The high-precision methods needed to create ultraprecise microcavities, used in for, example, diode lasers, are not required here. In addition, the materials can be produced on a large scale and have high emission efficiency. The main challenge for the development of future applications is that of electrical excitation of a random-laser material, which is crucial for display and lighting technology. Electrical conductance is going to be an important issue here, owing to the disordered and often porous character of the materials under study.

5.3 Conclusion

In this chapter, we demonstrated the random lasing behavior of a-plane ZnO/ZnMgO MQWs. At high excitation intensity (~55.7MWcm^{-2}), many sharp peaks

emerge on the spectra (Fig5.5). The FWHM of each individual peaks was about

0.37nm and the mode spacing was about 0.65nm. From Eq 5.2 we had calculated the

exciton binding energy is around 66meV which is closed to the activation energy. We

attributed this lasing behavior from the forming of electron-hole plasma and the

random lasing was achieved under the high excitation density. The threshold was

about 47.33MWcm^{-2}. For constant pump intensity of 113 MWcm^{-2}, larger excitation

area produces EHP lasing behavior easier. This is also a characteristic behavior in
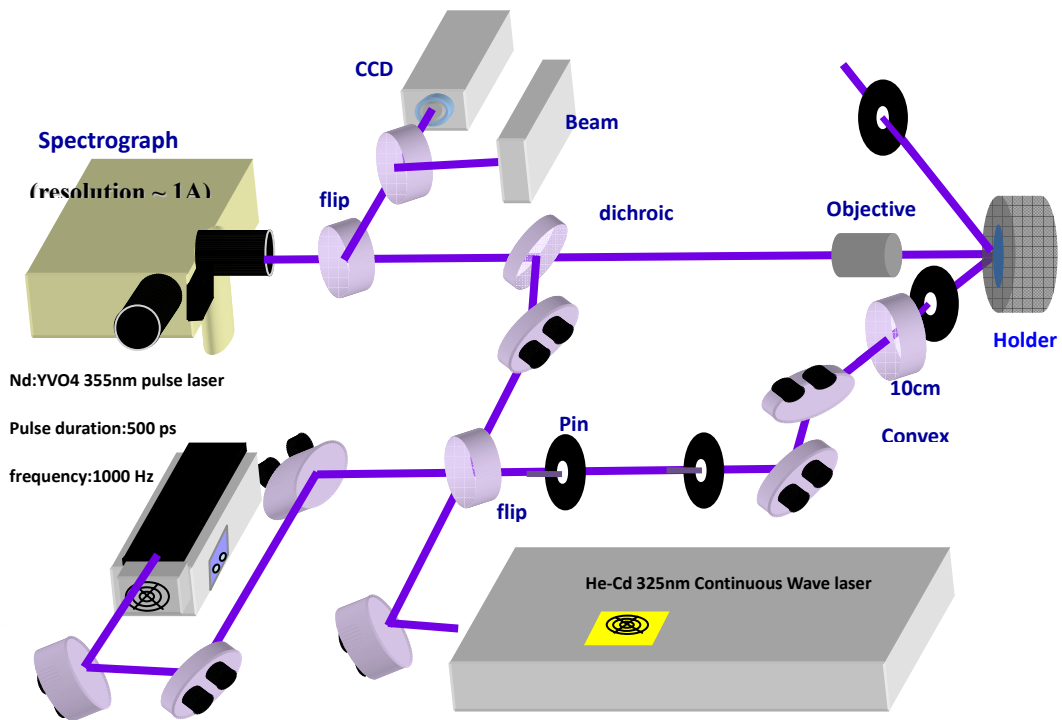
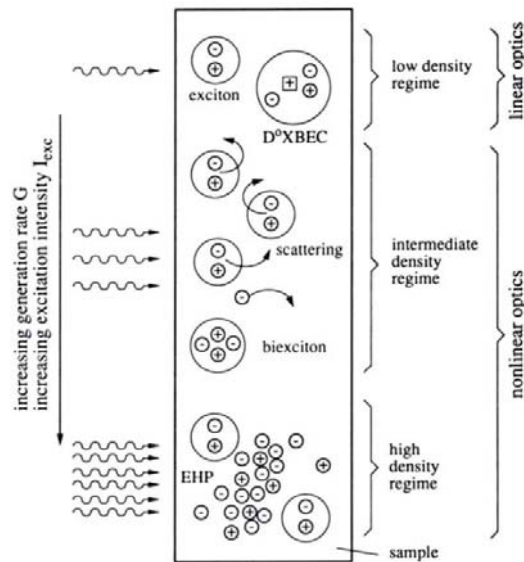random lasing system.

Fig5.1 Micro-PL system

Fig 5.2 A simple graph and the processes that occur with increasing excitation
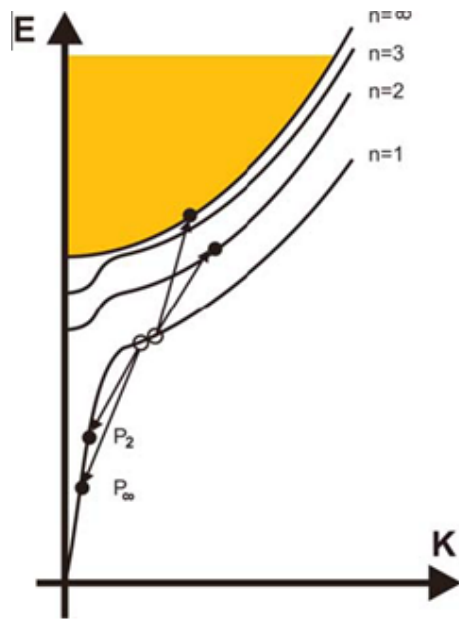
intensity.

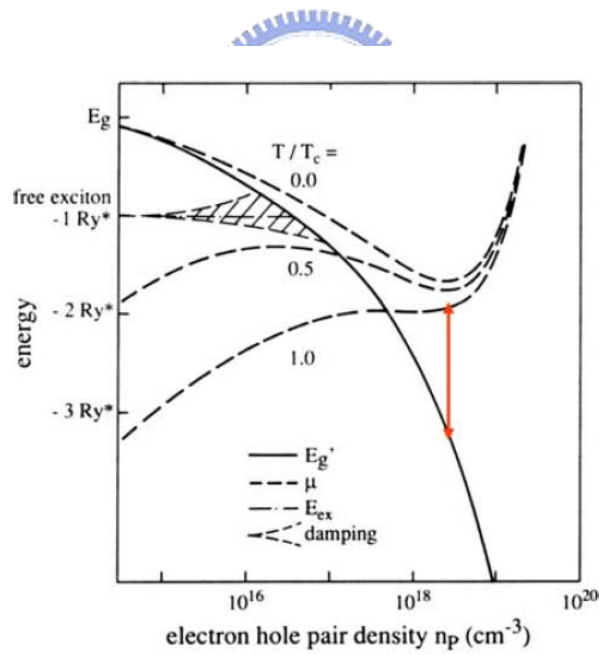Fig 5.3 A diagram of exciton-exciton scattering.

Fig 5.4 A function of the electron–hole pair density n_P the renormalization of the gap
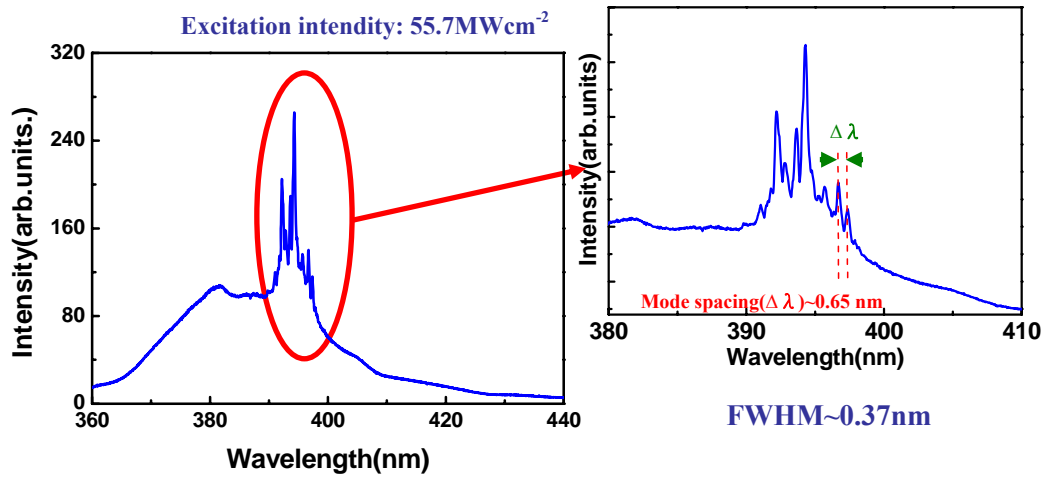
Fig5.5 The PL spectra at high excitation intensity.
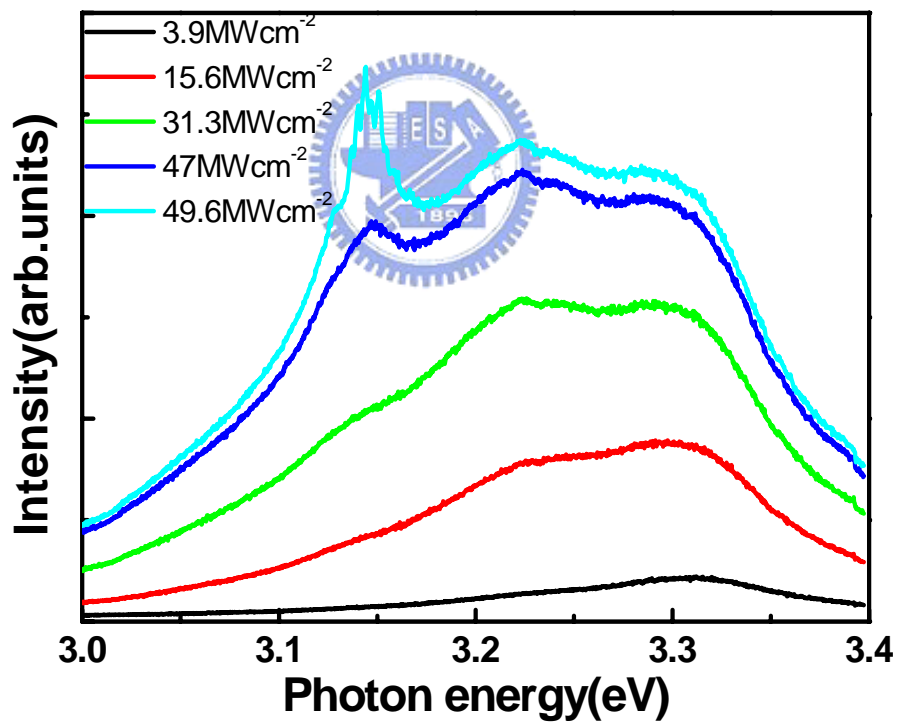

Fig5.6 Various spectra under different pumping intensity.
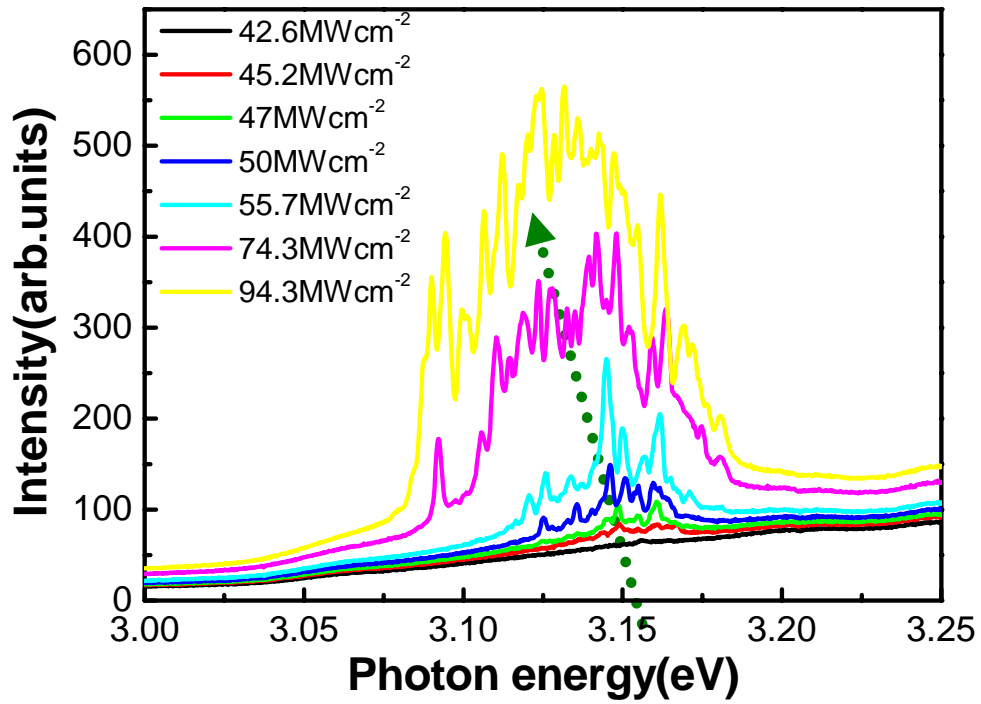
Fig5.7 Optical pumping measurement results.

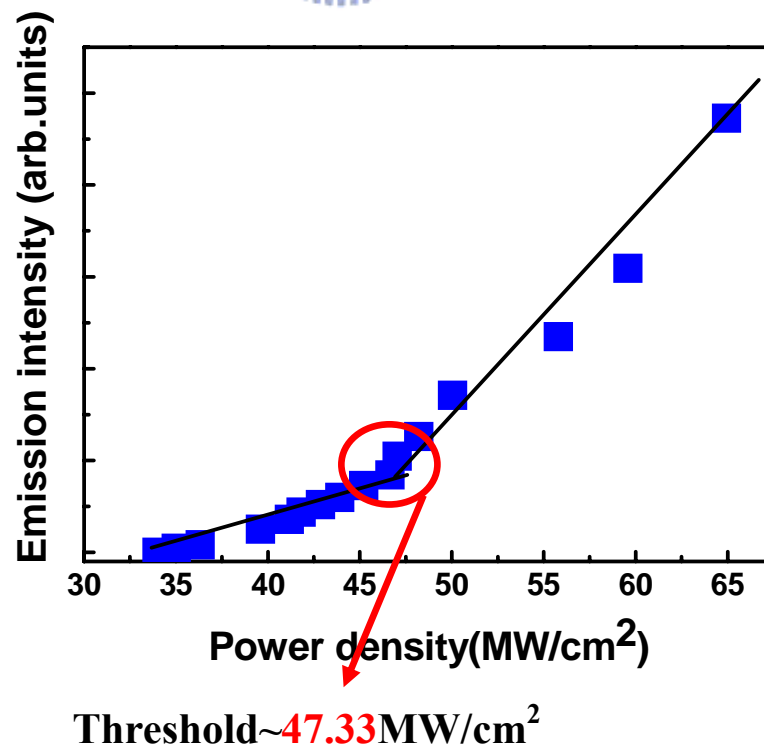
Threshold~**47.33**MW/cm^2
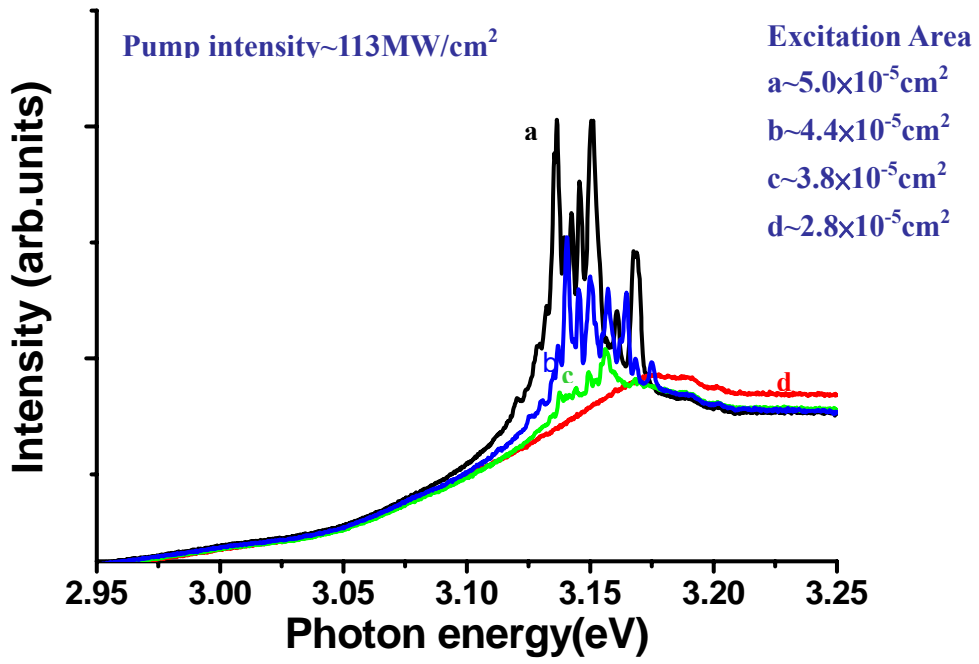
Fig5.8 The fitting result of lasing threshold.

Fig5.9 The evolution of the emission spectra when the excitation area was varied at a

fixed pump intensity.

Chapter 6 Conclusion and future work

6.1 Conclusion

In this thesis, a-plane ZnO/ZnMgO multiple quantum wells were grown on r-plane sapphire by pulsed laser deposition for investigation. From power-dependent PL measurement result, we observed the absence of a quantum-confined Stark effect, which is benefit to improvement of luminescence efficiency. Moreover, temperature dependent PL clearly show excitons confined in quantum well. From the fitting result of activation energy, the exciton binding energy was further enhanced by quantum well. High degree polarization ratio (92%) was observed in ZnO/$Zn_{0.8}Mg_{0.2}$O MQWs (@20K). From the polarized absorption spectra experiment results, electronic band structure was observed. Larger $\triangle E$ (E2-E1) was the main reason which induced high polarization ratio.

Further, we demonstrated the random lasing behavior of a-plane ZnO/ZnMgO MQWs. At high excitation intensity ($\sim 55.7 MWcm^{-2}$), many sharp peaks emerge on the spectra. The FWHM of each individual peaks was about 0.37nm and the mode spacing was about 0.65nm. From Eq 5.2 we had calculated the exciton binding energy is around 66meV which is closed to the activation energy. We attributed this lasing behavior from the forming of electron-hole plasma and the threshold was about $47.33 MWcm^{-2}$. For constant pump intensity of 113 $MWcm^{-2}$, larger excitaition area

produces EHP lasing behavior easier. This is also a characteristic behavior in random

lasing system.

6.2 Future work

In short, we have successfully grown the nonpolar ZnO/ZnMgO MQWs by

PLD and measured the optical characteristics. More effort to improve epitaxial crystal

quality and further design the structure of nonpolar ZnO/ZnMgO MQWs are needed

more study.

Reference

[1] T. Takeichi, S. Sota, M. Katsuragawa, M. Komori, H.Takeuchi, H. Amano, I.

Akasaki, Jpn. J. Appl. Phys. Part **2 36**, L382 (1997)

[2] M.D. Craven, P. Waltereit, J. S. Speck, and S. P. DenBaars, Appl. Phys. Lett. **84**,

496 (2004)

[3] D. M. Bagnall, Y. F. Chen, Z. Zhu, and T. Yao, M. Y. Shen and T. Goto, Appl. Phys.

Lett. 73. 1038 (1998).

[4] U. Woggon, Optical Properties of Semiconductor Quantum Dots (Springer, Berlin,

1997)

[5] J. K. Sheu, Y. K. Su, G. C. Chi, P. L. Koh, M. J. Jou, C. M. Chang, C. C. Liu, and

W. C. Hung, Appl. Phys. Lett., 74, 2340 (1999)

[6] S. Nakamura, T. Mukai and M. Senoh, Appl. Phys. Lett., 64, 1687 (1994)

[7] T. Someya, R.Werner, A. Forchel, M. Catalano, R. Cingolani, Y. Arakawa, Science, 285, 1905 (1999)

[8] C. C. Kao, Y. C. Peng, H. H. Yao, J. Y. Tsai, Y. H. Chang, J. T. Chu, H. W. Huang, T. T. Kao, T. C. Lu, H. C. Kuo, and S. C. Wang, Appl Phys. Lett., 87, 081105 (2005)

[9] T. Uenoyama, Phys. Rev. B, 51, 10228 (1995)

[10] Michael H. Huang, Samuel Mao, Henning Feick, Haoquan Yan, Yiying Wu, Hannes Kind, Eicke Weber, Richard Russo, Peidong Yang Science 292 189 (2001)

[11] Atsushi Tsukazaki, Akira Ohtomo, Takeyoshi Onuma, Makoto Ohtani, Takayuki Makino, Masatomo Sumiya, Keita Ohtani, Shigefusa F. Chichibu, Syunrou Fuke, Yusaburou Segawa, Hideo Ohno, Hideomi Koinuma and Masashi Kawasaki Nature Materials 4, 42 (2005)

[12] Sheng Chu, Mario Olmedo, Zheng Yang, Jieying Kong, and Jianlin Liu Appl. Phys. Lett. 93, 181106

[13] Morhain C et al 2005 Phys. Rev. B 72 241305

[14] Leroux M, Grandjean N, Laugt M, Massies J, Gil B, Lefebvre P and Bigenwald P 1998 Phys. Rev. B 58 R13371

[15] Gil B, Lefebvre P, Bretagnon T, Guillet T, Sans J A, Taliercio T and Morhain C 2006 Phys. Rev. B 74 153302

[16] Waltereit P, Brandt O, Trampert A, Grahn H T, Menniger J, Ramsteiner M,

Reiche M and Ploog K H 2000 Nature 406 865

[17] F. Bernardini, V. Fiorentini, and D. Vanderbilt, Phys. Rev. B **56,** R10024 (1997)

[18]T. Takeuchi, S. Sota, M. Katsuragawa, M. Komori, H. Takeuchi,H. Amano, and I.

Akasaki, Jpn. J. Appl. Phys. **36**, L382 (1997).

[19] P. Waltereit, O. Brandt, A. Trampert, H. T. Grahn, J. Menniger,M. Ramsteiner,

M.

Reiche, and K. H. Ploog, Nature 406, 865 (2000).

[20] Y. J. Sun, O. Brandt, S. Cronenberg, S. Dhar, H. T. Grahn, K. H. Ploog, P.

Waltereit, and J. S. Speck, Phys. Rev. B **67**. 041306 (2003)

[21] H. M. Ng, Appl. Phys. Lett. 80. 4369 (2002).

[22] H. M. Ng, A. Bell, F. A. Ponce, and S. N. G. Chu, Appl. Phys. Lett. 83, 653

(2003).

[23] M. D. Craven, P. Waltereit, J. S. Speck, and S. P. DenBaars, Appl. Phys. Lett.

84.

496 (2004).

[24] P. Waltereit et al., J. Cryst. Growth **437**. 227–228 (2001).

[25] M. D. Craven, S. H. Lim, F. Wu, J. S. Speck, and S. P. DenBaars, Appl. Phys.

Lett. **81**. 469 (2002).

[26] Y. J. Sun, O. Brandt, M. Ramsteiner, H. T. Grahn, and K. H. Ploog, Appl. Phys.

Lett. 82, 3850 (2003)

[27]B. Rau et al., Appl. Phys. Lett. 77, 3343(2000)

[28] C. Rivera, J. L. Pau, E. Muñoz, P. Misra, O. Brandt, H. T. Grahn, and K. H. Ploog, Appl. Phys. Lett. 88, 213507 (2006).

[29] K. Omae, T. Flissikowski, P. Misra, O. Brandt, H. T. Grahn, K. Kojima, and Y. Kawakami, Appl. Phys. Lett. 86. 191909 (2005).

[30] By Won Il Park, Gyu-Chul Yi, Miyoung Kim, and Stephen J. Pennycook Adv. Mater. 15. NO. 6 (2003)

[31] D. M. Bagnall, Y. F. Chen, Z. Zhu, T. Yao, M. Y. Shen and T. Goto Appl. Phys. Lett. 73, 1038 (1998)

[32] B. K. Meyer, H. Alves, D. M. Hofmann, W. Kriegseis, D. Forster,

F. Bertram, J. Christen, A. Hoffmann, M. Straßburg, M. Dworzak, U. Haboeck,

and A. V. Rodina Phys. stat. sol. (b) 241,NO. 2, 231~260

[33] Kazuto Koikea, Kenji Hama, Ippei Nakashima, Gen-you Takada, Ken-ichi Ogata, Shigehiko Sasa, Masataka Inoue, Mitsuaki Yano Journal of Crystal Growth 278 (2005) 288–292

[34] C. Morhain, T. Bretagnon, P. Lefebvre, X. Tang, P. Valvin, T. Guillet, B. Gil, T. Taliercio, M. Teisseire-Doninelli, B. Vinter, and C. Deparis Phys. Rev. B 72 241305(2005)

[35] Yong-Hoon Cho, G. H. Gainer, A. J. Fischer, J. J. Song, S. Keller, U. K. Mishra, and S. P. DenBaars, Appl. Phys. Lett. 73, 1370 (1998)

[36] A. Bell, S. Srinivasan, C. Plumlee, H. Omiya, F. A. Ponce, J. Christen, S. Tanaka, A. Fujioka, and Y. Nakagawa, J. Appl. Phys. 95, 4670 (2004)

[37] A. Yasan, R. McClintock, K. Mayes, D. H. Kim, P. Kung, and M. Razeghi, Appl. Phys. Lett. 83. 4083 (2003).

[38] M. Leroux, N. Grandjean, B. Beaumont, G. Nataf, F. Semond, J. Massies, and P. Gibart, J. Appl. Phys. **86**, 3721 (1999)

[39] C.X. Wu, Y.M. Lu, D.Z. Shen, Z.Z. Zhang, Z.P. Wei, Z.H. Zheng, J.Y. Zhang, Y.C. Liu, X.W. Fan J.ournal of Luminescence 122-123 405-407 (2007)

[40] G. Coli and K. K. Bajaj, Appl. Phys. Lett. 78, 2861 (2001)

[41] Yoon Sung Nam, Sang Wook Lee, K. S. Baek, S. K. Chang, Jae-Ho Song, Jung-Hoon Song, Seok Kyu Han, Soon-Ku Hong, and Takafumi Yao Appl. Phys. Lett. 92, 201907 (2008)

[42] C. Klingshirn phys. stat. sol. (b) 244, No. 9, 3027– 3073 (2007)

[43] C. Klingshirn. Semiconductor Optics, 3rd edn. (Springer. Heidelberg. Berlin, 2007).

[44] J. H. Hvam, Solid State Commun. 12, 95 (1973).

[45] C. Klingshirn, phys. stat. sol. (b) 71. 547 (1975).

[46] K. Bohnert, G. Schmieder, and C. Klingshirn, phys. stat. sol. (b) 98, 175 (1980).

[47] D. M. Bagnall, Y. F. Chen, Z. Zhu, and T. Yao S. Koyama, M. Y. Shen, and T. Goto Appl. Phys. Lett. 70. 2230 (1997)

[48] H. Cao, Y. G. Zhao, H. C. Ong, S. T. Ho, J. Y. Dai, J. Y. Wu, and R. P. H. Chang Appl. Phys. Lett. 73. 3656 (1998)

[49] Z. K. Tang, G. K. L. Wong, and P. Yu, M. Kawasaki, A. Ohtomo, and H. Koinuma, Y. Segawa Appl. Phys. Lett. 72. 3270 (1998)

[50] S. F. Yu, Clement Yuen,and S. P. Lau, Appl. Phys. Lett. 84. 3241 (2004)